**Impact of stress regime change on the permeability of a naturally fractured carbonate buildup (Latemar, The Dolomites, Northern Italy)**

Onyedika Anthony Igbokwe[1,2,*], Jithender J. Timothy[3], Ashwani Kumar[4], Xiao Yan[5,6], Mathias Mueller[1], Alessandro Verdecchia[1], Günther Meschke[6], Adrian Immenhauser[1,7]

Affiliation:

[1]Ruhr-University Bochum, Institute of Geology, Mineralogy and Geophysics, Universitätsstraße 150, 44801 Bochum, Germany

[2]Department of Physics, Geology and Geophysics, Alex Ekwueme Federal University Ndufu-Alike, Ikwo, P.M.B. 1010, Abakaliki, Ebonyi State, Nigeria

[3]Centre for Building Materials, Technical University of Munich, Franz-Langinger-Straße 10, 81245, Munich, Germany

[4]Advance Manufacturing Lab, ETH Zürich, Switzerland.

[5] Department of Geotechnical Engineering College of Civil Engineering, Tongji University, Shanghai 200092, China

[6]Ruhr University Bochum, Institute for Structural Mechanics, Universitätsstraße 150, 44801 Bochum, Germany.

[7]Fraunhofer IEG (Institution for Energy Infrastructures and Geothermal Systems), Lennershofstrasse 140, 44801 Bochum, Germany

* Corresponding author. Email: onyedikachi.igbokwe@rub.de

## Abstract

Changing stress regimes control fracture network geometry and influence porosity and permeability in carbonate reservoirs. We investigate the impact of stress-regime change on fracture network permeability utilizing outcrop data analysis and a displacement-based linear elastic finite element method. The model is based on fracture networks, specifically, fracture sub-structures. The Latemar, predominantly affected by subsidence deformation and Alpine compression, is taken as an outcrop analogue for isolated (Mesozoic) carbonate buildups with fracture-dominated permeability. We apply a novel strategy involving two compressive boundary loading conditions, constrained by the NW-SE and N-S stress directions in the study area. Stress-dependent heterogeneous apertures and effective permeability were computed by: (i) using the local stress state within the fracture sub-structure and (ii) running a single-phase flow analysis considering the fracture apertures in each fracture sub-structure. Our results show that the impact of the modelled far-field stresses at: (i) subsidence deformation from the NW-SE, and (ii) Alpine deformation from N-S, increased the overall fracture aperture and permeability. In each case, increasing permeability is associated with open fractures parallel to the orientation of the loading stages and with fracture densities. The anisotropy of permeability is increased by the density and connectedness of the fracture network and affected by of shear dilation. The two far-field stresses simultaneously acting within the selected fracture sub-structure at a different magnitude and orientation do not necessarily cancel out each other in the mechanical deformation modelling. These stresses effect the overall aperture and permeability distributions. These effects, which may be ignored in simpler stress-dependent permeability, can result in significant inaccuracies in permeability estimation.

## 1. Introduction

Naturally fractured reservoirs accommodate a significant share of the world's hydrocarbon resources, especially in carbonates that contain between 50 – 60% of oil and gas reserves worldwide (Garland et al., 2012). These reservoirs also play an essential role in the transition to a low carbon energy future, especially in producing low- and high-enthalpy geothermal heat or sequestering $CO_2$ (McNamara et al., 2015). However, these potentials have not been fully explored partly because of the challenge in predicting and quantifying the contribution of fluid flow through fractures in naturally occurring complex fracture networks (Berkowitz, 2002; Narr et al., 2006). The challenge is primarily due to the sub-seismic heterogeneous characteristics of fractures, partially studied from core data or image logs (Laubach, 2003), and the lack of an understanding of the structural arrangement of the fracture networks and their 3-D distribution and geometrical attributes. Given that core data or image log (capturing small-scale or local information around a well) lacks information on the spatial arrangement (Bourbiaux et al. 2005), outcrop analogues are often used for explicit descriptions of fracture distributions, including length, orientation, spacing and aperture (Agosta et al., 2010; Bonnet et al., 2001; Hooker et al., 2013; Igbokwe et al., 2018, 2020; Wilson et al., 2011). Integrated and detailed outcrop studies provide constraints for understanding most fracture geometrical parameters because analogues have adequate resolution over a varied length scale of $10^{-1}$ – $10^{4}$ m, even in the 3-D (Rotevatn et al., 2009; Igbokwe et al., 2020). Also, outcrop analogues can be extrapolated to reservoir scale fracture models based on geomechanical relations as long as the data are accurately captured and corrected for sampling artefacts (Bisdom et al., 2016; Narr et al., 2006).

In many natural reservoirs, the fractures act as the principal pathways for fluid or gas flow, particularly in low matrix permeability rocks. Fracture aperture is one of the main factors controlling fracture flow, as the aperture delineates fracture porosity and permeability (Bisdom et al., 2016; Hooker et al., 2013). Minor variations in aperture have enormous implications on rock flow and transport properties (de Dreuzy et al., 2002; Matthäi, 2003; Matthäi & Belayneh, 2004), and obtaining a realistic aperture prediction from outcropping geometries is challenging. At depth, in-situ stresses partly control aperture, which influences permeability by either increasing or decreasing their order of magnitude (Lei et al., 2015, 2017; Zoback, 2007), but pressure relief during exhumation and weathering effects dissolve occluded fractures and change the aperture. Thus, the outcropping aperture cannot be considered representative, except when these apertures are generated from veins that have not been reactivated during exhumation (e.g., Hooker et al., 2013, 2014). Having said that, preserved veins covering a large outcrop scale equivalent to a reservoir scale are rarely found in nature.

As an alternative, fracture aperture is modelled as a function of stress (shear stress-induced dilations), using hydromechanical coupling based on linear elastic fracture mechanics (Bisdom et al., 2017; Lei et al., 2015; Min et al., 2004). These models require the local stress state, typically derived from Finite Element (FE) models with explicit fracture representations (Bisdom et al., 2016; Lei et al., 2017). The local state of stress can change the hydraulic properties and fluid pressure and vice versa in a rock domain. For stress-induced changes in hydraulic properties, permeability can be several orders of magnitude and irreversible under perturbations resulting from various natural activities. These activities can cause stress redistribution, such as in geothermal energy and oil/gas reservoir production, where injections and extractions of fluids demand meaningful change in effective stresses underground (Min et al., 2004). Thus, investigating the impact of stress change on permeability becomes fundamental in understanding the reservoirs' overall aperture distribution and flow pattern.

The effect of stress on the permeability of fractured rocks has been widely investigated using synthetic fracture networks and 2-D fracture network models. For example, the level of differential stress considerably impacted the magnitude and direction of rock mass permeability when the stress effects on the 2-D permeability tensor of three sampled natural fracture networks were analyzed (Zhang & Sanderson, 1996). Min et al. (2004) observed significant stress-induced flow enhancement along with connected shear fractures in the study of stress-dependency of rock mass permeability with the effects of non-linear joint normal deformation and shear dilation. While Bisdom et al. (2016) investigated the influence of in-situ stress on the permeability of an outcrop-based fracture system, Lei et al. (2014) analyzed the stress effect on the validity of synthetic fracture networks for representing a naturally fractured rock in terms of geomechanical and hydraulic properties.

These previous studies mainly considered the tectonic stress perturbation based on a single stress regime that differently scrutinizes the magnitude and orientation of principal stresses on a rock body. However, past studies did not necessarily consider the different tectonic episodes that build up different stress regimes, and which may change in geological time. In nature, the stress in a rock body can exist in two forms (i) the far-field stress impacting the rock from outside the body and (ii) the local state of stress domiciled inside the rock body. The far-field stress is of tectonic origin, or related to lateral pressure changes affected by the lateral thickness and density variations (Pascal & Cloetingh, 2009). At the same time, the local state of stress is characterized by rotations and changes in principal stress orientations, magnitude, and so on, all taking place inside the rock body. The local state of stress changes is linked to the impact of far-field stresses and geometry, distribution and density of fracture network characteristics. Therefore, investigating stress perturbation and its effects on the permeability of rock bodies need a comprehensive approach that will capture the impact of the magnitude and orientation of the far-field stresses and the associated changes in the local state of stress in different tectonic episodes.

The difficulty is primarily representing: (i) the stress-regime changes over time, (ii) the complex fracture system geometry, having various orientations and lengths, and (iii) the complex mechanical deformation mechanism, influencing the interactions between individual fractures in a FE mechanical model. Until now, a focused study dealing with the superposition of different magnitude and direction of the far-field stresses, representing the major geological tectonic episodes in a given area, has not been well-represented in several FE mechanical models. As such, the overall impact of stress-regime change on permeability remains poorly understood.

In this study specifically, we investigate the influence of the superposition of two orthogonal far-field stresses, derived from significant tectonic episodes, on the permeability of the carbonate rocks with different fracture distributions. Natural fracture geometry with multiple fracture sets and intersections from an outcrop analogue at the Latemar carbonate platform was utilized. The two major tectonic events that occurred at Latemar are associated with subsidence-related deformation in Late Triassic and Early Jurassic times, shortly after the fractures were formed, and later Alpine compression during the Neogene. Although new fractures may have formed during these tectonic episodes, we assumed that new fractures did not form and/or grow in the model used in this study. Instead, already developed fractures were either opened and/or closed during these tectonic events. This enables us to study stress regime change effects on permeability, focusing on those issues related to the complexity of multiple fractures. The development of the Latemar fractures and their driving factors, including their geometries, connectivities etc., is beyond this paper's scope and has been discussed in detail in Igbokwe et al. (2022). Our goal is to draw general conclusions about the overall impact of stress regime change on permeability in complex fractured systems representing an analogue of the subsurface reservoirs.

The main objectives of this paper are to (i) analyze the selected fracture network characteristics of the study area, to (ii) evaluate the impact of stress regime change, considering the overall tectonic episodes, to (iii) compute the stress-induced fracture aperture in a FE model, and to (iv) evaluate the changes in the effective permeability and permeability anisotropy. The implication of the central assumptions and the impact of the changing stress orientation and magnitude on effective permeability are discussed.

## 2. Geological background and study area

The Latemar carbonate platform is one of the pre-volcanic Middle Triassic isolated carbonate platforms (Goldhammer & Harris, 1989; Preto et al., 2011) located in the southwestern part of the Dolomite Mountain belt (Northern Italy; Fig. 1), and neighboured by the Catinaccio and the Agnello platforms in the north and south, respectively (Fig. 1a). The outcrops of the Latemar are built predominantly by the Sciliar (Schlern) Formation (Fig. 1b), underlying the Contrin Formation, which is a regionally important carbonate bank in the Dolomite Mountain belt (Gaetani et al., 1981; Jacquemyn et al., 2014). Between the Late Anisian and Late Ladinian (Middle Triassic), the Latemar platform formed on topographic highs. Their buildups were separated by basinal areas where siliceous, basinal carbonates were deposited (Fig. 1; Bosellini, 1984).

The Latemar has a maximum altitude of 2850 m, with high peaks exposing the platform margin, the slope and the interior (Fig. 1c, d). While the preserved portions of the platform margin consist of reefal boundstones, microbial crust, and marine cement-facies, the slope is characterized by massive breccia flows, including coarse and matrix-poor materials derived from the platform margin or platform interior (Egenhoff et al., 1999; Emmerich et al., 2005; Goldhammer & Harris, 1989; Harris, 1994; Marangon et al., 2011). The platform interior is arranged in dm's-to m's-scale shallowing upward cycles (Christ et al., 2012; Goldhammer et al., 1990), consisting of up to 750 m successions of subtidal and peritidal carbonate lagoonal deposits. The Latemar platform was partly dolomitized as a consequence of fluid mobilization triggered by the activity of the Predazzo Volcanic-Plutonic Complex in the Middle Triassic. A recent review on the dolomitization and diagenesis of the Latemar platform is given by Mueller et al. (2021).

The considered outcrop in the presented study area is a large fractured pavement in the platform interior (Fig. 1c, d). The studied pavement ( *ca*. 7.5 x $10^2$ $m^2$) consists of limestone and dolostone rock bodies, showing a gentle dip of fewer than $5^o$ towards the north. Most structural features observed on the fractured pavements are fractures, veins and stylolites, some of which are weathered.

### 2.1. Tectonic setting

The Latemar forms part of the Southern Alps, part of the Mesozoic Adriatic plate, predominantly thrusting southward during the Alpine collision (e.g., Boro et al., 2013; Doglioni, 1988). Deposition in the Latemar began on a structural high (horst) generated by extensional tectonics, breaking up the widespread regional carbonate bank (Contrin Fm.). Subsequently, subsidence deformation and extensional synsedimentary tectonics controlled the geometry of the platform, leading to faulting. Several fractures and/or faults crosscut the Latemar platform, formed in conjugate pairs and are related to Middle Triassic subsidence deformation. Besides, Preto et al. (2011) documented the ENE-WSW and WNW-ESE faults linked to the Triassic trans-tensional regime as the oldest fault direction in the Latemar. The outcome is a platform with a horseshoe shape and intraplatform basins (Fig. 1a, c; Preto et al., 2011). Dextral strike-slip reactivation, observed along magmatic dikes, reflects Neogene Alpine compressional tectonics in the Latemar. Before the Neogene compressional tectonics, a regional magmatic-tectonic event in the Late Ladininan to Early Carnian triggered intense magmatic activity. These generated the intrusion of the Predazzo Volcanic-Plutonic Complex and the Mt. Monzoni, which are associated with temporarily halting carbonate deposition at Latemar (Bellieni et al., 2010; Bosellini, 1984; Bosellini et al., 2003).

In the Latemar platform, two principal far-field stresses did affect the carbonate deposits, representing the two main phases of deformation, namely: NW-SSE (Middle Triassic extensional (subsidence) tectonics) and the N-S (Alpine compressional tectonics) (Boro et al., 2013; Hardebol et al., 2015; Jacquemyn et al., 2015; Preto et al., 2011).

## 3. Methodology

The methodology applied includes a-three phase workflow with (i) drone image acquisition and outcrop interpretation and digitization (Fig. 2a), (ii) meshing and geomechanical finite element aperture modelling and calculations (Fig. 2b), and (iii) fluid-flow modelling and effective permeability calculations for uncoupled hydromechanical conditions.

### 3.1. Outcrop acquisition and digitization

Fracture network patterns from the outcropping carbonate rocks in the sub-horizontal pavements of the flat-topped Latemar interior platform were acquired using drone imagery (DJI Phantom 4®). The acquired images were processed using Agisoft Metashape® and converted into georeferenced digital outcrop models using photogrammetry.

The observed fractures were interpreted and digitized using ArcGIS 10.5™ software, where fractures were traced and digitized with a polyline interpretation tool. Structural data such as length, orientation and spacing were computed for each polyline. The high quality of the drone images allows interpretations of thousands of potential fractures. In total, more than 2000 fractures were documented.

Although the drone image covers most areas with a relatively high resolution, these data sets still include a limited number of sampling and truncation artefacts. Additionally, drone images were used to guide detailed fieldwork on the ground to document minute structural details that were only in part visible in drone images. Aside from the sub-horizontal outcrops, bedding perpendicular outcrop stations, ranging from a few m's to 10's meters, were also studied in the nearby Valsorda Valley. This provides information that enabled the documentation of the paleostress fields affecting the entire buildup.

Within the 2-D digitized fracture network of the sub-horizontal outcrop, five representative fracture network areas, referred to as fracture sub-structures (FSS), were selected and used to model stress heterogeneity and permeability. The dimensions of the individual FSS are approximately 2 x 2 m. For each FSS, the fracture length distributions and frequencies were fetched from the digitized fractures and plotted in a histogram chart. The FSS areas are located in the same structural domain, but they display fracture networks with different spatial distributions. Further, fracture networks were commonly sub-vertical, splaying, curving, intersecting and tipping adjacent to other fractures. Locally, the fractures are orthogonal and/or in a conjugate pattern with a small conjugate angle. Slight modifications and/or extrapolations of the fracture's original pattern were implemented to maintain the fracture topological connectivity.

### 3.2. Stress and permeability modelling

The acquired 2-D fracture network was simplified and meshed to model the impact of stress regime change and fracture topology on the permeability of the fractured carbonate rock, using selected FSS (FSS 1 through FSS 5) in the manner described below.

First, the selected digitized fracture geometry was converted to 2-D 'element geometry' and meshed into a triangular mesh using GiD[1] (a geometric modelling and mesh generation software for pre-and post-processing). The GiD converts the vector images into meshes using triangular elements, and fractures were specified as interface elements (Fig. 2b; Phase 2.1). A complete geometrical topology was ensured by defining additional interface elements not corresponding to the fractures. This provides an accurate representation of fracture connectivity and topology, which is essential, especially when the matrix of the fractured rock is close impermeable (Hardebol et al., 2015; Sanderson & Nixon, 2015). Further, the mesh was refined to avoid singularities issues to capture complex geometries where high variations were expected, especially around the fracture tips and corners. Finally, these meshes were read directly into the FE simulator to analyze the stress distribution in a complex fracture network.

Second, 2-D linear-elastic mechanical finite element analyses were conducted using KRATOS open-source geomechanical software. The 2-D linear-elastic mechanical modelling

[1] **GiD** is a universal, adaptive and user-friendly **pre** and **post processor** for numerical simulations in science and engineering. https://www.gidhome.com/ (Accessed May 24, 2022)

was achieved by applying loads and/or displacement boundary conditions to the models (Fig. 2b; Phase 2.2). The applied boundary conditions approximate the impact of the two tectonic episodes (far-field stresses) within the study area that affected the complex fracture network shortly after the fractures were formed. These tectonic episodes are the subsidence-related deformation, having a sub-horizontal NW-SE shortening direction and the later Alpine deformation with a N-S compression direction. We assume their maximum magnitudes as 50 and 160 MPa for subsidence-related- and Alpine deformations, respectively. A 2-D plane strain linear elastic isotropic matrix was assumed for the presented models. The 2-D plane strain was used in order to treat all modelled fracture planes equally, especially on the *z*-axis.

The stress distributions were analyzed using continuum triangular elements and interface elements, corresponding to the rock matrix and fractures. The effects of the far-field stresses on the overall model and the relative displacement of the deformed and undeformed element geometries were stimulated. Given that all FSS are sub-horizontal, the origin of the *x* and *y*-axis is placed at the centre of the plane. In other words, a homogenous Dirichlet boundary condition was applied at the centre of the FSS, i.e., assuming the centre to be fixed in either *x*- or *y*-axis so that translation and rotation are prevented. After the specified Dirichlet boundary, a sequential Neumann boundary (applied loading) condition followed. The Neumann boundary application utilized the direction and magnitude of the two major tectonic (stress) episodes in the study area, on each selected FSS. The loading of the first tectonic episode, subsidence deformation, represented as first stage loading, was applied from the NW-SE direction and increased in discrete steps until a maximum magnitude of 50 MPa was reached. After that, the loading of the second tectonic stage, Alpine compression and known as second stage loading, was added (or applied) from the N-S direction, while the compressive loading corresponding to the first stage was active and/or maintained at 50 MPa. Analogous to stage 1 loading, the load values were increased in discrete steps until a maximum value of 160 MPa was attained (Fig. 2b; Phase 2.2.1). The applied boundary loading is analogous to in-situ stresses, which are feasible magnitudes for modelling compressive settings (Heidbach et al., 2018). The essential model parameters are listed in Table 1. The modelled local state stresses and slips were used to calculate the local stress-induced aperture and their distributions, even as individual fractures open differently.

Third, the permeability was calculated by conducting a single-phase flow simulation in two perpendicular directions, using a computational homogenization (Leonhart et al., 2017) for an unperturbed and a perturbed fracture state. The permeability tensors of the deformed carbonates were obtained. We simulated (i) uncoupled hydromechanical modelling scenarios were simulated, (ii) applied fluid pressure as a surface pressure to the sidewall of the FSS, (iii) we run simulations using linear FE solver, and (iv) post-processed outputs the use in flow simulations.

### 3.3. Stress-dependent aperture

Stress-dependent apertures describe the opening of fracture planes, as compressive loads are applied within a fracture system. In the geomechanical FE model (Fig. 2b; Phase 2.3), stress-dependent apertures were calculated from the shear stresses. As represented in the model, the shear stresses resulting from the impact of the two primary loading conditions and changes in apertures were documented within each loading scenario.

In the model, the interface elements were inserted in sections, which are not considered as fractures. However, these interface elements are closed, behaving like the rock matrix, and were inserted into the simulation purely for computational reasons. Interface elements corresponding to the fractures obtained from the digitizing procedure were allowed to only open and/or close. The initial aperture size of these interface elements was assumed to be zero. The interfaces corresponding to the rock matrix were filtered out of the aperture dataset because the 'aperture' values corresponding to these interfaces are always zero. Since we did not allow new fractures to form, the interface elements were not activated, thus maintaining zero aperture values.

## 4. Finite Element Analysis (FEA)

A displacement-based linear elastic finite element method (FEM) was used to solve linear poroelasticity equations over the domain of interest. In this section, the fractures and the rock matrix are considered in the uncoupled hydromechanical numerical modelling. The fractures are regarded as having zero-thickness interface elements embedded into the rock space, as shown in figure 3a.

The balanced equation for the porous medium according to the general Biot's theory can be written

$$\nabla \cdot \boldsymbol{\sigma} + \rho \mathbf{b} - \rho \ddot{\mathbf{u}} = 0 \tag{1}$$

where $\sigma$ is the total stress tensor, $\mathbf{b}$ is the body force, $\ddot{\mathbf{u}}$ is the acceleration vector of the solid and $\rho$ is the density of the porous medium.

The saturated single-phase flow in both the fractures and rock matrix obeys Darcy's law and can be calculated based on a mass conservation equation:

$$\frac{\partial}{\partial t}(\phi^{\tau}\rho_w) + \nabla \cdot (\rho_w \dot{\mathbf{w}}_{\mathbf{m}}) = \rho_w q_s$$

where $\tau$ is a sign expressing the different media in the model domain, for example, $\tau = m$ expressing a matrix and $\tau = f$ expressing a fracture, where $\varphi^m$ is the porosity of the rock matrix, and $\varphi^f$ is the porosity of a fracture, $\rho_w$ is the density of the fluid, $q_s$ is the source term, $\varepsilon_{vol} = \nabla \cdot \mathbf{u}$ denotes the velocity of the solid matrix and $\dot{\mathbf{w}}_{\mathbf{m}}$ is the Darcy velocity vector of the pore fluid, which can be written as:

$$\dot{\mathbf{w}}_{\mathbf{m}} = \frac{1}{\mu}\mathbf{k}^{\tau} \cdot \nabla p \tag{3}$$

where $\mathbf{k}_{\tau}$ is the intrinsic permeability tensor for rock matrix and fracture, which is replaced by a scalar value $k$ for the isotropic medium, and $\mu$ is the fluid viscosity. According to the cubic law, the intrinsic fracture permeability can be calculated as

$$k^f = \frac{w^2}{12} \tag{4}$$

where $w$ is the fracture aperture.

### 4.1. Governing equations

A two-dimensional porous media domain $\Omega$ bounded by the boundary $\Gamma$ is necessarily considered to obtain the governing equations. As depicted in figure 3b, a fluid-filled geomechanical discontinuity $\Gamma_d$ is contained in the porous medium.
The essential boundary conditions are imposed on the external boundary as the prescribed primary variables:

$$\mathbf{u} = \bar{\mathbf{u}} \quad \text{on } \Gamma_u \qquad p = \bar{p} \quad \text{on } \Gamma_p \tag{5}$$

and the natural boundary conditions are imposed on the external boundary as the prescribed traction and volume flux:

$$\boldsymbol{\sigma} \cdot \mathbf{n}_{\Gamma} = \bar{\mathbf{t}} \quad \text{on } \Gamma_t \qquad \dot{\mathbf{W}} \cdot \mathbf{n}_{\Gamma} = \bar{q} \quad \text{on } \Gamma_q \tag{6}$$

where $\bar{\mathbf{t}}$ is the prescribed traction applied on the boundary $\Gamma_t$; $\bar{q}$ is the prescribed flux imposed on the permeable boundary $\Gamma_q$, and $\mathbf{n}_\Gamma$ is the unit outward normal vector to the external boundary.

### 4.2. Discretization model

This section presents the computational framework of the numerical modelling and the method to estimate the effective permeability of fractured rock medium. It is essential to note that stress-dependent permeability of a fractured rock domain is governed by dilatation of the fractures. In this model, the coupling problem includes two parts: the hydraulic solver, which solves the fluid pressure during the fluid process, and the mechanical solver, which calculates the deformation of the rock matrix and evaluates the fracture open and closure.

#### **4.2.1.** *Fluid discretization*

The fluid flows through the same 'conduit systems' in the fluid solver, which can be regarded as matrix conduits and fracture conduits. As shown in figure 4, the interface element is a 6-node quadrangle. The fluid flows between the mid-plane nodes of the interface element (see node 5 and node 6 in Fig. 4a), which can be seen as the flow fracture (conduit). The degree of freedom (dof) of fluid pressure is added to node 5 and node 6.

The equations for fluid flow through the control volume of a node are derived by formal integration methods, such as the finite volume method (FVM), expressed as follows:

$$\int_V \frac{\partial \rho_w \phi^\tau}{\partial t} dV + \int_A \mathbf{n} \cdot (\rho_w \cdot \dot{\mathbf{w}}_{\mathbf{m}}) = \int_V \rho_w q_s dV \tag{7}$$

In this model, the 2D fracture segment can further be simplified as a 1D line called fracture conduit, denoted with $fp(i,j)$, which is associated with two end nodes $i$ and $j$, as shown in figure 4b. Each node represents a half volume of the fracture ($wl/2$). If the fluid pressures are known in the end nodes, the flow rate in the fracture can be evaluated by the difference equation:

$$Qfij = Kijf\,(pi - pj) \tag{8}$$

where $K_{ij}^f$ is an equivalent conductance coefficient of the fracture conduit, which can be calculated by:

$$K_{ij}^f = \frac{w^3}{12\mu l_{ij}} \tag{9}$$

For an effective simulation of fluid flow in a porous medium, the porous medium is reconstructed using an equivalent fracture network graph. The volume of the porous medium is discretized and represented by nodes. The equivalent hydraulic parameters of the fractures are derived based on the unstructured triangular mesh.

For the derivation of the parameters of fractures, forming a triangular mesh, the circumcenter ***o*** of the triangle is selected as its division point (Fig. 4c). The line linking the circumcenter and the mid-point of each edge is perpendicular to the edge, and these perpendicular bisectors divide the triangle into three parts. The equivalent conductance coefficient of the matrix conduit *mp*(*i*,*j*) is derived from unstructured triangular elements, as shown in figure 4c. The volume of each fracture node is half the volume of the triangle, which is composed of the two fracture nodes (node *i* and *j*) and the circumcenter (node *O*).

In the porous medium, when the fluid is transferred (between node *i* and *j*), the fluid flows between domain *ogif* and domain *oejf* through their common face *of*. Thus, the flow rate $Q_{ij}$ in the fracture *mp*(*i*,*j*) is equal to the flow rate

$Q_{of}$.

$$Qmij = Kijm(pi - pj) \tag{10}$$

$$Q_{of} = -\frac{k}{\mu}\int_{of} \nabla p \cdot \mathbf{n}_{of} dl = \frac{kl_{of}}{\mu l_{ij}}(p_i - p_j) \tag{11}$$

Thus, the equivalent conductance coefficient $K_{ij}^{m}$ can be calculated by:

$$K_{ij}^{m} = \frac{kl_{of}}{\mu l_{ij}} \tag{12}$$

The equivalent conductance coefficient of flow fracture is the sum of the fracture conductance coefficient $K^f$ and matrix conduit conductance coefficient $K^m$, which can be expressed as:

$$K_c = K^f + {}^{X}K^m \tag{13}$$

For each node *i*, the governing equation for single-phase saturated flow in the rock matrix and fractures are expressed as:

$$\frac{\partial \rho_w \phi^\tau V_i^\tau}{\partial t} + \rho_w \sum_{j=1}^{n_i} K_{ij}^{\tau}(P_i - P_j) = \rho_w Q_{s_i} \tag{14}$$

### **4.2.2.** *Mechanical discretization*

In the mechanical solver, the fluid pressure on the fracture surface is governed by

$$p_{\Gamma_d^-} = p = p_{\Gamma_d^+} \tag{15}$$

Thus, the pressure on node 1 and node 3 is equal to that on node 5, and the pressure on node 2 and node 4 is equal to that on node 6 (Fig. 4a).

The weak form of the equilibrium equation for the porous fractured medium is given as:

$$\int_\Omega (\boldsymbol{\sigma}' - \alpha \mathbf{m} P) : \nabla \delta \mathbf{u} \, d\Omega + \int_{\Gamma_d} [\![\delta \mathbf{u}]\!] (\mathbf{t}_d - P \mathbf{n}_{\Gamma_d}) \, d\Gamma_d = \int_{\Gamma_t} \delta \mathbf{u} \cdot \bar{\mathbf{t}} \, d\Gamma_t + \int_\Omega \delta \mathbf{u} \cdot \mathbf{b} \, d\Omega \tag{16}$$

The discrete displacement field and the pore pressure field in the rock matrix are approximated by:

$$\mathbf{u} = \mathbf{N}_u \mathbf{U}$$
$$p = \mathbf{N}_p \mathbf{P} \tag{17}$$

where **U** and **P** are the nodal displacement and pressure; $\mathbf{N}_u$ is the matrix of shape functions, and $\mathbf{N}_p$ is the row vector of shape functions. It is assumed that the same shape functions adopted for both **u** and $p$ are reasonable.

$$\int_\Omega (\boldsymbol{\sigma}' - \alpha \mathbf{m} P) : \nabla \delta \mathbf{u} \, d\Omega + \int_{\Gamma_d} [\![\delta \mathbf{u}]\!] (\mathbf{t}_d - P \mathbf{n}_{\Gamma_d}) \, d\Gamma_d = \int_{\Gamma_t} \delta \mathbf{u} \cdot \bar{\mathbf{t}} \, d\Gamma_t + \int_\Omega \delta \mathbf{u} \cdot \mathbf{b} \, d\Omega \tag{18}$$

The displacement jump across the fracture and the pressure field in the fracture can be expressed as:

$$[\![\mathbf{u}]\!] = \mathbf{R} \mathbf{N}_{int} \mathbf{U}_{int}$$
$$p_f = \mathbf{N}_f \mathbf{p}_f \tag{19}$$

where **R** is the rotation matrix; $\mathbf{N}_{int}$ is the matrix of shape functions in the interface element and $\mathbf{N}_f$ is the row vector of shape functions in the interface element.

According to the Eq.16, the discrete equation for the mechanical part is given as:

$$\int_\Omega \mathbf{B}_u^T \cdot \boldsymbol{\sigma}' \, d\Omega - \mathbf{C}_{uw} \mathbf{P} + \int_{\Gamma_d} \mathbf{N}_{int}^T \mathbf{R}^T \mathbf{t}_d \, d\Gamma - \mathbf{C}_{int} \mathbf{P} = \int_{\Gamma_t} \mathbf{N}_u^T \bar{\mathbf{t}} \, d\Gamma + \int_\Omega \mathbf{N}_u^T \mathbf{b} \, d\Omega \tag{20}$$

where $\mathbf{B}_u$ is the strain-displacement ($\varepsilon - \mathbf{u}$) matrix and it can be expressed as:

$$\varepsilon_u = \mathbf{B}_u \mathbf{u} \tag{21}$$

the matrices $\mathbf{C}_{uw}$ and $\mathbf{C}_{int}$ are given by

$$\mathbf{C}^{uw} = \int_\Omega \alpha \mathbf{B}_u^T \mathbf{m} \mathbf{N}_p \, d\Omega \tag{22}$$

$$\mathbf{C}^{int} = \int_{\Gamma_d} \mathbf{N}_{int}^T \mathbf{R}^T \mathbf{m}_2 \mathbf{N}_f \, d\Gamma \tag{23}$$

where $\mathbf{m} = \{1\ 1\ 0\}^T$ and $\mathbf{m}_2 = \{1\ 0\}^T$.

In this mechanical solver, the pressure acting on the fracture surface is regarded as an external force. Thus, Eq.20 can be rewritten as:

$$\mathbf{KU} = \mathbf{F}^{ext} \tag{24}$$

where $\mathbf{K}$ is the stiffness matrix and $\mathbf{F}^{ext}$ is the vector of external force:

$$\mathbf{K} = \mathbf{K}^{bulk} + \mathbf{K}^{int} \tag{25}$$

with

$$\mathbf{K}^{bulk} = \int_\Omega \mathbf{B}_u^T \mathbf{D} \mathbf{B}_u \, d\Omega \tag{26}$$

$$\mathbf{K}^{int} = \int_{\Gamma_d} \mathbf{N}_{int}^T \mathbf{R}^T \mathbf{T} \mathbf{R} \mathbf{N}_{int} \, d\Gamma \tag{27}$$

$$\mathbf{F}^{ext} = \int_{\Gamma_t} \mathbf{N}_u^T \bar{\mathbf{t}} \, d\Gamma + \int_\Omega \mathbf{N}_u^T \mathbf{b} \, d\Omega + \mathbf{C}_{uw}\mathbf{P} + \mathbf{C}_{int}\mathbf{P} \tag{28}$$

### 4.3. Effective permeability for fractured rock and aperture modelling

This section provides algorithms for the effective permeability $k_{eff}$ of fractured rock. For a 2D square domain with randomly distributed fractures, the effective permeability for different flow directions $k_{xx}$ and $k_{yy}$ is different. $k_{xx}$ is solved by applying pressure boundary conditions ($p_1 \neq p_2$) at the left and right boundaries and zero fluid flow conditions ( $q = 0$ ) at the top and bottom boundaries, while applying pressure boundary conditions at the top and bottom boundaries and zero fluid flow conditions at the right and left boundaries for $k_{yy}$. Having computed the fluid flow $q$ through the fractured rock domain through Equation.14, the effective permeability is estimated as:

$$k_{eff} = \frac{\mu L}{(p_1 - p_2)W} \sum_{i=1}^{m} q_i \tag{29}$$

where $m$ is the number of total points on the fluid injection boundary, $L$ is the length of the domain in the direction of fluid flow, and $W$ is the width of the domain.

## 5. Numerical experiments on a single fracture impact on effective permeability

This experiment evaluates the behaviour of the effective permeability $k_{xx}$ and $k_{yy}$ under different fracture aperture values for uncoupled hydromechanics processes. In essence, this experiment aims to validate the consistency of the computed effective permeability values (results) with varying aperture sizes in the models. For this reason, numerical experiments are simulated, in this section in a selected rock domain with a single fracture, by choosing a range of intrinsic matrix permeability and fracture apertures, such as $10^{-9}$, $10^{-15}$, and $10^{-21}$ $m^2$ and 0.001, 0.01, 0.1, 1, and 10 mm, respectively.

The matrix permeability values are drawn from Latemar mean platform permeabilities estimated from forward-coupled modelling of the sedimentary and diagenetic evolution in Whitaker et al. (2014). In contrast, the aperture sizes are arbitrarily chosen, reflecting a logarithm range. The permeability $k_{xx}$ corresponds to the permeability computed by applying a pressure gradient in the horizontal direction. In contrast, the permeability $k_{yy}$ corresponds to the permeability calculated by applying a pressure gradient in the vertical direction. By 'uncoupled', we mean that fluid flow cannot cause the deformation of the rock matrix and does not influence the opening and closure of fractures.

Constraining the simulation within the rock domain to a single fracture in the rock matrix, figure 5 shows the simulation of effective permeability under different inclination degrees for a single fracture across the rock matrix, such as $0^o$, $45^o$ and $90^o$.

It is observed that the existence of a single fracture has little influence on the effective permeability of the rock domain when the permeability of the fracture is less than that of the rock matrix. This means that the fracture aperture is small, i.e., when $w < \sqrt{12\, k_m}$. Also, if the fracture in the rock matrix is parallel to the x- and as well to the y-axis, $k_{yy}$ and $k_{xx}$ assume constant values, the same as the intrinsic matrix permeability (Fig. 5a – c), respectively.

## 6. Results

The workflow presented in figure 2 is applied to model the aperture and permeability distributions through an outcropping network of fractures. Further, the two (quasi-static) loading scenarios, representing the boundary loading conditions (or far-field stresses), are highlighted. Extracting five selected outcrops (e.g., FSS1 – FSS5) from the fractured pavement, outcrop models developed demonstrate in more detail the impact of the mechanical deformation (loading), change in stress regimes and fracture geometry on modelled aperture and effective permeability. Also, the flow anisotropy function in response to the loading scenarios and orientation is evaluated.

### 6.1. Field data and fracture network geometry analysis

Field investigation of Latemar outcrops shows widespread brittle deformation features with low strain barren fractures and veins as the dominant structures. These features are displayed as mode I, conjugate hybrid fractures, and stylolites. By considering the prominent sub-vertical outcrops exposed at the base of the Latemar (in the Valsorda Valley; Fig. 6) and sub-horizontal (pavement) outcrops at the flat-topped Latemar buildup (Fig. 7), the arrangements, orientations and the stress fields during the development of the fractures are documented.

In the Valsorda Valley (Fig. 6), carbonate outcrops are affected by minor reverse conjugate faults dipping at low-angle (< 30º) to bedding. These conjugate reverse faults strike between *ca* 238º WSW-ENE and 250º SW-NE, accommodating low-angle SSE - and ENE dipping fractures with a horizontal intersection. The movement of these faults and associated tectonic stylolites correspond to NNW-SSE compression. On the other side, at the flat-topped Latemar, on the sub-horizontal (pavement) outcrops, fractures also form conjugate patterns, exhibiting dextral and sinistral displacements (Figs. 7 and 8). These fractures documented from the field and drone images highlight the NNW-SSE, NE-SW and ENE-WSW orientations as the dominant fracture set and record an approximately NE-SW compression (Fig. 8b). The measured sub-vertical stylolites show the primary orientation of WNW-ESE and strike perpendicular to the bisection planes of the observed conjugate systems (Figs. 6 and 7c).

Here, we focused on the sub-horizontal (pavement) outcrops, where figure 8b shows embedded five representative FSS. Each FSS contains a sufficient number of fracture heterogeneities to give a representative value of a property such as fracture densities, spacing, connectivity etc. Geometrical analysis of the outcrops indicates that while average length varied between 0.5 and 3.5 m, in all the selected FSS, fracture density (P20) is similar in FSS1, FSS2 and FSS3 (10.5 $m^{-2}$, 21 $m^{-2}$, 13.3 $m^{-2}$), and dissimilar across FSS4 and FSS5 (62.3 $m^{-2}$ and 42.5 $m^{-2}$) (Fig. 8d, e). The average fracture spacing (in each FSS) for each fracture orientation range between 0.7, 0.72 and 0.4 m for NNW-SSE, NE-SW, and ENE-WSW, respectively (Fig. 8e). The dihedral angles between the different fracture orientations measure between 18 and 60º.

The overall results show two deformation phases, falling in the reverse fault and strike-slip stress regimes with sub-horizontal σ1 striking approximately NW-SE to NNW-SSE and NE-

SW, respectively (Figs. 6 through 8). A later compressive deformation stage with a stress regime showing largely N-S sub-horizontal σ1 was also observed. These stress regimes and orientations correlate well to the far-field sub-horizontal σ1 observed for the Latemar mountains during the Middle to Late Triassic and Neogene times, representing the subsidence – and Alpine deformation stages, respectively (Boro et al., 2013, 2014; Hardebol et al., 2015; Igbokwe et al., 2022). The orientation of these stress regimes supports the boundary loading directions defined in the modelling work presented here. Also, during the modelling, we assumed that all fractures, including stylolites, can be re-used as fluid-flow conduits. Although stylolites tend to hinder fluid flow (Boersma et al., 2019), observations in figures 6 and 7 show they can enhance fluid movement.

### 6.2. Boundary loading conditions

The boundary conditions defined by two stages of far-field stress loading scenarios are presented in figure 9. The first and second loading scenarios, corresponding to the far-field sub-horizontal σ1 (stress), acted on the studied carbonates forming the Latemar buildup during the subsidence and Alpine deformation stages, respectively. The first stage of loading, acting from the NW-SE direction, gradually reaches a maximum loading condition at 50 MPa in Time Step 1.0 (Time Steps here are analogues to quasi-static loading; Fig. 9a, c). Line a-b-c (blue curve) represents this stage in figure 9c. The Line d-e-f (orange curve) depicts the second stage loading, which acts from the N-S direction and gradually reaches a maximum value of 160 MPa in Time Step 2.0 (Fig. 9b, c). It is essential to note that the second loading stage was added when the first stage loading reached the maximum magnitude of 50 MPa, and while the first stage loading was still active, the addition of the second stage loading continued until a maximum magnitude of 160 MPa was reached (Fig. 9c). Figure 9c shows the graph of the Load (MPa) versus Time Steps, and the grey bar represents the transition zone between the two loading scenarios.

### 6.3. Stress orientation effects and aperture distributions

The local distributions of stresses and the computed aperture distributions from local state of stress are presented. The effects of changing stress regimes, from NW-SE and N-S directed stress cases, for each of the FSS domains are shown in figure 10, demonstrating the distributions of Von-Mises stress in all the FSS due to applied loading conditions. At the onset of the subsidence stage, a uniform distribution of local stress state at Time Step 0.01 is observed. This uniform distribution of local stress increases gradually until Time Step 1.0 is reached. At Time Step 2.0 (Alpine deformation stage), the increasing loading in the N-S direction shows the disperse of the uniform stress distribution with noticeable fluctuations in magnitudes, pointing to the varied change in the local state of stress caused by the heterogeneity of fractures (Fig. 10).

Figure 11 shows the displacement magnitude distribution when the loading conditions are at Time Step 2.0 in each FSS. The observations in figures 10 and 11 document how changes of the sub-horizontal far-field stresses and their magnitude cause varied deformation and/or influence the individual fractured rock domain, the FSS. These changes, particularly in figure 11 are, however, quantified for each FSS, as ranging from 0 – 0.012 m (FSS1), 0 – 0.079 m (FSS2), 0 – 0.080 m (FSS3), 0 – 0.034 m (FSS4) and 0 – 015 m (FSS5). It is observed that the total displacement magnitude in the model increases with increased fracture density and connectivity. For example, FSS2 and FSS3 show a slight increase in the displacement magnitude due to increased fracture density and intersection (Figs. 8e and 11).

Depending on the magnitude and orientation of the loading scenarios, fractures open, close and/or shear. Fracture apertures and their overall distributions against the number of fractures for each FSS are shown in figure 12. The aperture values vary between 2 and 40 mm, showing distinct heterogeneous apertures of variable sizes within each FSS (Fig. 13a). Quantifying the changes in aperture as a function of increasing stress and changing stress orientations for each FSS, figure 12b shows the general trend of aperture distribution. For instance, in each FSS, a rapid increase in aperture value was observed as the first loading in the NW-SE direction increased, and this value peaked at Time Step 1.0 (at 50 MPa). At the second loading stage in the N-S direction, the trend of aperture values changes. For example, in this case, FSS 1, 4 and 5, the aperture values initially decrease rapidly until Time Step 1.3 is reached. After that, aperture trends remained constant for FSS 4 and 5, whereas FSS 1, 2 and 3 aperture values gradually increased until reaching their peak values at Time Step 2.0 (160 MPa; Fig. 13b).

### 6.4. Effective permeability as a function of loading

The effective permeability, in each of the FSS, is presented as a function of the NW-SE and N-S loading scenarios. Fracture apertures mechanically generated were applied to the finite element models, and by running the single-phase flow simulations, the effective permeabilities for each loading condition (stress orientation) were obtained. For a 2 x $10^{-15}$ $m^2$ matrix permeability, the flow is calculated based on the fracture densities and orientations in all the

FSS. The flow paths are linked to the areas where there is a high number of fractures. Figure 13 shows a nearly homogenous long-term steady-state fluid pressure distribution and gradients over the fractured rock domain (FSS) at the quasi-static loading of Time Step 2.0 in the x- and y-directions. This result points to the steady-state condition of the pressure field, serving as the base from which the effective permeabilities of all the selected FSS were computed.

In addition, using the parameters in Table 1 and considering the initial fracture aperture to be zero, figure 14 show the computed effective permeabilities in both x and y directions (the red curve = $k_{xx}$ and the black curve = $k_{yy}$). Also, the components of the permeability tensor for each loading condition are shown in Table 2.

The results from the first loading stage (Time Step 1.0; representing the subsidence deformation stage from the NW-SE direction) show a gradual increase in permeability beyond the matrix permeability within each FSS (Fig. 14). The increased permeability values correspond to increased aperture values in figure 12b, pointing to the initial opening of most fractures parallel to the NW-SE direction. On the other side, for the second loading stage (Time Step 2.0), for which the loading is applied from the N-S while the first loading stage is active, the permeability values are seen to increase in varying degrees. While the close fractures have reduced aperture and permeability values, opened fractures exhibit increased permeability values (Figs. 12b and 14). Further, in both loading scenarios, a general observation shows that the permeability values are variable in each FSS, pointing to the random distribution of fractures, varied densities (Fig. 8) and varied aperture values (Fig. 12a). For instance, in loading stage 1 from the NW-SE orientation, the results in the permeability plots show both the vertical and horizontal permeabilities increase gradually in FSS 1 through FSS 5 (Fig. 14).

Although FSS 1, FSS 2 and FSS 5 have their permeability values (in both x- and y-direction) close to the matrix permeability, FSS 3 and FSS 4 only show permeability values increased by 55 and 70 % in comparison to the matrix permeability (Table 2). But, with the second loading scenario from the N-S orientation, the $k_{xx}$ and $k_{yy}$ maintained a relatively steady permeability value with a slight increase in FSS 3 through FSS 5. This is unlike FSS 1 and FSS 2, which recorded a sharp increase (a jump) in both $k_{xx}$ and $k_{yy}$.

Quantitatively, the average permeability for all the FSS is given as 2.75 x $10^{-15}$ $m^2$ and 2.64 x $10^{-15}$ $m^2$ in the x- and y-direction for Time Step 1.0, and 2.77 x $10^{-15}$ $m^2$ and 3.24 x $10^{-15}$ $m^2$ in the x- and y-direction for Time Step 2.0, respectively. When compared to the matrix permeability, these average permeability values, $k_{xx}$ and $k_{yy}$, increased by 37.5 and 32% for Time Step 1.0 (at the maximum magnitude of 50 MPa in the subsidence stage) and 38.5 and

62% for Time Step 2.0 (at the maximum magnitude of 160 MPa during the Alpine deformation stage).

## 7. Interpretation and Discussion

The results of the structural analysis and geomechanical (numerical) simulations show how stress regime change can impact the permeability of a naturally fractured carbonate rock. In addition, this process can be the first step toward using fractures (and faults) as a flow medium. This is especially true for the upscaling and larger-scale numerical simulations that are important for fluid flow in geothermal and hydrocarbon systems.

### 7.1. Subsidence- and Alpine deformation: establishing a realistic loading condition for the Latemar buildup

Deformation in the carbonates of the Latemar buildup caused the development of different sets of fracture networks, including veins. As documented before, these fracture networks formed during syn-sedimentary extension tectonics in the Middle Triassic, characterized by wholesale subsidence deformation and faulting tectonics (Boro et al., 2013; Preto et al., 2011). Other studies (e.g., Goldhammer and Harris, 1989; Emmerich et al., 2005) suggest that the subsidence deformation in Latemar may have continued until Late Triassic or Early Jurassic times. Thereafter, the Latemar platform was affected by the Alpine deformation between the Late Paleogene and Early Neogene times. These tectonic episodes significantly impacted the hydraulic properties of fracture networks at the Latemar.

Given the complexities of the modelling work presented here, the studied fracture networks were assumed to have formed earlier prior to the major tectonic episodes, as documented in Preto et al. (2011). Although both tectonic events may have developed new fractures, the modelled tectonic stresses in this study did not allow for further development of fractures but for fractures to open, shear and/or close, consequent on the orientation of the stresses.

Our structural analysis results (Figs. 6 and 7) reveal the orientation of the principal stress fields affecting the fractures at the subsidence and extension tectonic stage, which is roughly NW-SE to NNW-SSE trending sub-horizontal $\sigma1$ and a sub-vertical $\sigma3$. This compression is believed to have taken place at a relatively shallow to an intermediate burial depth. Indirect evidence for this notion comes from the understanding that, in the presence of sub-horizontal tectonic stress, a sub-vertical position of $\sigma3$ is compatible with low-angle reverse faults (or structures), forming at shallow to intermediate burial depth (e.g., Fig. 6; Bisdom et al., 2016;

Bertotti et al., 2020). This means that at the subsidence stage, the overburden stress is the resultant far-field stress with an approximate NW-SE orientation and a magnitude of 50 MPa. On the other side, the main Alpine deformation in the Dolomite Mountain Belt (including the study area) involved maximum compressive stress (σ1) orientated approximately N-S with a magnitude estimated at 160 MPa (Peacock, 2009; Abbà et al., 2018). Because the observed correlation between the fractures (and their networks) and stress fields are largely clear, the magnitude of the two sub-horizontal σ1 served as the input parameters for the numerical mechanical modelling phases, i.e., the mechanical loads used during the mechanical FE model setup. These mechanical loads captured the realistic compressive boundary condition, reflecting the tectonic episodes of the study area, unlike previous studies (e.g., Zhang and Sanderson, 1996) and are essential for the realistic computation of effective permeabilities, even at the subsurface.

Figure 9c reveals that the deformation caused by the first stress field (NW-SE shortening direction at subsidence stage) was still active, as the second stress field (N-S sub-horizontal σ1; Alpine deformation) was added. The gap (the grey bar Fig. 9c) between the two stresses in our model signifies that some stresses in the horizontal dimension due to subsidence deformation are present (active) at the Alpine deformation stage when they increase and become more extensive in the N-S direction. This is in contrast with previous studies, for example, Stephansson et al. (1991) and Yale (2003), where modelling results (or model setup) utilize a homogenous stress regime that does not account for all other stress impacts around the fracture network. In the cases where all the stress regime changes are considered, each stress regime's effect remains independent from each other (Agheshlui et al., 2018; Bisdom et al., 2017). That is, the impact of the first or second stress field, as the case may be, is not kept active when the third or fourth stress field is implemented. Unique to our study, the orientation and magnitude of all the stress regimes, reflecting the major tectonic event over a geological period, are kept active and accounted for during the geomechanical modelling. Thus, making the impact of stress irreversible in a given rock domain, without which it can pose significant uncertainty in the computation of effective permeability at the subsurface reservoir scale level. This argument follows the proponent of representing the realistic tectonic events affecting fracture networks on the geomechanical models. Thus, proposing that modelling the impact of different tectonic episodes (in our case, the subsidence- and Alpine deformation) on a given rock domain (FSS, in the Latemar platform) over a geologic time (Triassic to Neogene) will significantly reduce uncertainties in computing the apertures and permeabilities, even at the reservoir scale.

Based on this, the loading conditions and the calculated permeabilities presented in figures 9 and 14 may reflect close occurrences of what is obtainable at the subsurface of a natural carbonate reservoir.

### 7.2. The link between heterogeneous aperture, fracture geometry and the impact of stress and effective permeability

As a rule, the geomechanical models and flow simulations in fractured rocks have always depended on: (i) the subsurface datasets, which are typically expensive, albeit with uncertainty ranges (Bourbiaux et al., 2002; 2005), and (ii) stochastic datasets (Khodaei et al., 2021; Timothy & Meschke, 2016), which are not realistic when considering the behavior of a fracture network in a natural reservoir. In contrast to these studies, the presented investigation solely uses the outcropping network geometry as input for geomechanical and flow models, not considering the outcropping apertures. Instead, the geomechanical aperture sizes were modelled in a representative outcrop fracture network using computational homogenization (FE mechanical modelling) for unperturbed and perturbed fracture states. The natural fracture system is perturbed by applying mechanical load, analogous to in-situ stress.

The combination of outcrop fracture geometries, mechanical loading and aperture distribution results in models that are more representative of fractured reservoir permeability compared to analogues studies that use apertures of exhumed barren fractures or assume a constant aperture for the whole fracture network (Bisdom et al., 2017; Makedonska et al., 2016). Like most fractured reservoir models, the aperture is assumed constant per fracture or even per fracture set because generating a reservoir scale 3-D fracture model with mechanically controlled heterogeneous aperture distributions can be a complex task (Geiger and Matthäi, 2014). However, studies by Jonoud and Jackson (2008) and Cottereau et al. (2010) have given an upscaling alternative through arithmetic or harmonic averaging of the explicit fracture permeability model calculated per fracture node. That is, the mechanically controlled heterogeneous aperture, just like the mechanically generated aperture in figure 12, can easily be upscaled to serve a more representative reservoir scale fracture model.

Further, fracture networks, including intensely fractured zones, are believed to significantly influence the effective permeability and fluid flow patterns in a naturally fractured reservoir, particularly in tight carbonate reservoirs. These network areas show high porosities and permeabilities relative to the surrounding host rock (Bruhn et al., 2017; Matthäi, 2003). It is a widely held view that the extent to which the fracture networks impact flow lies in the fracture's structural arrangement and geometry, such as fracture orientations, spacing, and length (Bisdom et al., 2016; Hardebol et al., 2015; Olson, 2003; Scholz, 2010). However, these views are limited to models that quantify aperture based on fracture length and spacing relations (Olson, 2003; Scholz, 2010). The results from our models (Figs. 12 and 14) indicate that aperture and effective permeability are not easily related to fracture geometrical parameters such as length or spacing. This is especially true because the linear functions of fracture lengths and spacing have little or no effect on the mechanically generated aperture distribution (Bisdom et al., 2016), controlled by fracture orientation and the impact of stress.

Given these results, we suggest that the distribution of aperture and permeability (in the presented models) is influenced by the impact and direction of the stresses, fracture orientation and shear displacement (Figs. 12 and 14). For the stress-induced aperture, the mechanical load opens individual fractures orthogonal to the direction of loading at different rates and, at the same time, closes the fractures parallel to the loading direction (Heffer & Koutsabeloulis, 1995). Therefore, in a favorable orientation, that is, the direction with significant stress components (of mechanical loading), which in our case is NW-SE for the subsidence deformation, the results show a considerable increase in permeability as the load increases (Fig. 14) before reaching a peak at Time Step 1.0. The increased permeability is beyond the matrix permeability within all the FSS. On the other side, permeability continues in an upward trajectory with varying degrees of increased values (Fig. 14) in the direction of more significant stress components (N-S), at the Alpine deformation stage, for all the FSS, until a maximum loading value is reached.

The evolution of permeability values in x- and y-directions within the FSS indicates that the values of the permeability distribution are variable. These variabilities are linked to the varied fracture densities and aperture values (Fig. 8). In fractured reservoirs, apertures of natural fractures are highly heterogeneous and can contribute to the induced anisotropy in the permeability (Makedonska et al., 2016). In our case, for instance, FSS 1, FSS 3, and FSS 5 significantly differ in the evolution of the permeability values in the x- and y-directions and distinctly show induced anisotropy in the permeability within their rock domains (Fig. 14). This is demonstrated by the differences in the permeability values in x- and y-directions. The higher the difference in the permeability values of the x-and y-direction, the more significant the induced anisotropy. These differences are linked to the fracture connectivity and/or distributions (Fig. 8c, d) within each FSS. Conversely, FSS 2 and FSS 4 show isotropy in permeability, as the differences in the permeability values of x- and y- directions are relatively small compared to the differences in FSS 1, FSS 3, and FSS 5. These behaviours can be explained as follows; initially, during the subsidence stage, when the far-field stress (or compressive loading) is in the NW-SE direction, the fractures parallel to this direction open while the fractures orthogonal to the NW-SE direction close. The opening of the NW-SE-directed parallel fractures increases the overall permeability in all FSS (Fig. 14). However, at Time Step 1.0, the second set of loading scenarios is gradually applied from the N-S direction at the onset of Alpine deformation. While the loading from the first stage is kept constant, the overall permeability at this stage continues with varying degrees of the increase until Time Step 2.0. This implies that the new loading opens the fractures parallel to the N-S direction and closes the fracture orientation in the E-W direction (Fig. 14). Hence the second loading stage, in principle, opens the fractures that were previously closed by the first loading stage. Meaning that a significant number of fractures opened, resulting in larger permeability values. There is also a documented sharp jump in permeability values for FSS 1, FSS 2 and FSS 3 at the beginning of the second loading stage. This sharp increase in the permeabilities may imply that fractures oriented slightly in the NE-SW and/or NW-SE directions (Fig. 8c) may have been opened by the N-S loading condition.

In addition, fracture density and/or the number of fractures in each rock domain, FSS, may have played a considerable role in the sharp spike in permeability values. For example, in FSS 1 and FSS 2, where the quick jump in permeability values is predominant, fracture density is relatively low than in FSS 4 and FSS 5, with high fracture density and no visible sharp increase. These explain the jump and the overall increase in permeability during the second loading stage. Recent studies have linked the fracture density, the number of fractures and the stress orientation with an overall increase in the permeability values (e.g., Bisdom et al., 2016; Furtado et al., 2022). Although some fractures may have been sheared and eventually opened during loading, we believe that the shearing of these fractures has minimal or no impact on the overall permeability of the rock domains.

One interesting observation in this research investigation is that the two far-field stresses acting within a rock domain at a different magnitude and orientation at the same time (in our case at Time Step 2.0) do not necessarily cancel out each other in the mechanical FE modelling phases. But these stresses create new effects on the overall aperture and permeability distributions. In our case, a general increase in the overall aperture and permeability values, respectively (Figs. 12b and 14).

### 7.3. Implications

All modelled features are assumed as reactivated fractures that control the fluid flow in the presented numerical workflow. Because of the effects of weathering and exhumation, the distinction between open fractures, veins, stylolites and shear fractures was not made. Although this assumption is widely used in reservoir modelling, complex features such as sub-vertical (tectonic) stylolites or partly cemented fractures can inhibit or enhance fluid flow (Bruna et al., 2019). Cemented fractures strongly constrain fluid flow, as cementation reduces the aperture of a fracture plane (Gale et al., 2010; Olson, 2007).

Although our study permits investigating the impact of stress regime change in detail, the results will broadly differ in complex and large-scale reservoirs since our model is orders of magnitude smaller than a subsurface reservoir. The studied fracture networks have relatively simple geometries on a small scale compared to what is usually observed in large-scale reservoirs. However, Matthai and Nick (2009) and Bisdom et al. (2016a) upscaled heterogeneous aperture distribution to a single averaged aperture, which provided the same permeability distribution. This means that averaging and upscaling the permeability of small-scale fracture models can accurately describe permeability when most fracture contributes to flow. Otherwise, the small-scale models may not be representative.

Another issue is ignoring the influence of the overburden stress on fracture aperture. Overburden stresses result in lateral expansion of rock layers and, in addition to the horizontal stresses, fracture apertures are strongly dependent on overburden stresses due to Poisson's effect (Agheshlui et al., 2018). Therefore, conducting the numerical analysis in 2-D constrains the effects of lateral expansion of fractured rocks domain, which can displace the rock body and increase the fracture aperture. This means that the results presented in our model may only provide indicative approximations.

Lastly, having a better knowledge of stress conditions and elastic parameters aids the prediction of realistic aperture descriptions for reservoir models. Studies have noted the impact of these parameters on modelled stress-induced aperture such that stress orientations and the magnitude of differential stress largely influenced the resulting aperture distribution (Agheshlui et al., 2018; Bisdom et al., 2016a). The presented model assumed the magnitudes of the two stress regimes following the calculated palaeostress in other field areas with the same geodynamic conditions. The values of these magnitudes are debatable and subjective. Therefore, changing the magnitude of these stress values can affect this study's overall aperture and permeability distributions. Still, the workability of the model remains stable and can compute any given matter.

## 8. CONCLUSIONS

A detailed workflow is presented that applies a displacement-based linear elastic finite element method (FEM) to solve linear poroelasticity equations to model the impact of stress regime change on the permeability of carbonate rock. By considering the tectonic episodes (Subsidence- and Alpine deformations) and outcropping fracture network at the Latemar, the stress-induced heterogeneous aperture distribution was generated in the selected Fracture Sub-structure (FSS). The impact of stress regime change on flow was quantified in terms of varied aperture and effective permeability. Although the studied fracture networks have relatively simple geometries compared to what is ordinarily observed in reservoir scale, this permits investigating the impact of individual stress magnitude and stress regime change on the permeability.

First, a numerical experiment was simulated using a synthetic single-fracture in a rock matrix domain to validate the consistency of the effective permeability values with the chosen varying aperture sizes. By choosing a range of intrinsic matrix permeability and fracture apertures, the results show that a single fracture has little influence on the effective permeability of the rock domain when the permeability of the fracture is less than that of the rock matrix.

Second, we presented the structural analysis and interpretation of fracture network geometry in the study area, considering the two major tectonic episodes, the subsidence – and Alpine deformation. Their stresses were considered far-field stresses (compressive loading), which informed the boundary conditions (two loading stages) in the geomechanical FE modelling. The first stage of loading acts from the NW-SE direction, representing the subsidence deformation and gradually reaches a maximum loading condition at 50 MPa in Time Step 1.0, whereas the second loading stage, the Alpine deformation, was superimposed on the first and gradually reached a maximum value of 160 MPa in Time Step 2.0.

It was shown that in the directions with less significant stress components (of mechanical loading), NW-SE, the overall permeability increased gradually within all the FSS as the load increased before reaching a peak at Time Step 1.0. In addition, permeability increase continues with the upward trajectory in the direction with more significant stress components (N-S) for all the FSS as the load increases. Fracture density, the number of fractures and the stress orientation play a critical role in the overall increase in the permeability values.

Finally, we conclude that the two mechanical loadings simultaneously acting within a rock domain at a different magnitude and orientation do not necessarily cancel out each other in the mechanical FE modelling phases. However, these mechanical loads create new effects in the overall aperture and permeability distributions, which can be complicated in large subsurface reservoirs.


## Acknowledgements

The Petroleum Technology Development Fund (PTDF) Abuja, Nigeria, is thanked for sponsoring the doctoral fellowship of the first author (Grant number: OSS/PHD/IOA/843/16). The authors are grateful to N. Gründken and S. Schurr for their assistance during the fieldwork. Many thanks to J. Dikachi-Igbokwe for her helpful comments, which helped improve this paper.


## 9. REFERENCES


Abbà, T., Breda, A., Massironi, M., Preto, N., Piccin, G., Trentini, T., Bondesan, A., Carton, A., Fontana, A., Mozzi, P., Surian, N., Zanoner, T., & Zampieri, D. (2018). Pre-Alpine and Alpine deformation at San Pellegrino pass (Dolomites, Italy). *Journal of Maps*, *14*(2), 683–691. https://doi.org/10.1080/17445647.2018.1536001

Agheshlui, H., Sedaghat, M. H., & Matthai, S. (2018). Stress Influence on Fracture Aperture and Permeability of Fragmented Rocks. *Journal of Geophysical Research: Solid Earth*, *123*(5), 3578–3592. https://doi.org/10.1029/2017JB015365

Agosta, F., Alessandroni, M., Antonellini, M., Tondi, E., & Giorgioni, M. (2010). From fractures to flow: A field-based quantitative analysis of an outcropping carbonate reservoir. *Tectonophysics*, *490*(3–4), 197–213. https://doi.org/10.1016/j.tecto.2010.05.005

Bellieni, G., Fioretti, A. M., Marzoli, A., & Visonà, D. (2010). Permo-Paleogene magmatism in the eastern Alps. *Rendiconti Lincei*, *21*(SUPPL. 1), 51–71. https://doi.org/10.1007/s12210-010-0095-z

Berkowitz, B. (2002). Characterizing flow and transport in fractured geological media: A review. *Advances in Water Resources*, *25*(8–12), 861–884. https://doi.org/10.1016/S0309-1708(02)00042-8

Bisdom, K., Nick, H. M., & Bertotti, G. (2017). An integrated workflow for stress and flow modelling using outcrop-derived discrete fracture networks. *Computers and Geosciences*. https://doi.org/10.1016/j.cageo.2017.02.019

Bisdom, Kevin, Bertotti, G., & Nick, H. M. (2016a). The impact of in-situ stress and outcrop-based fracture geometry on hydraulic aperture and upscaled permeability in fractured reservoirs. *Tectonophysics*. https://doi.org/10.1016/j.tecto.2016.04.006

Bisdom, Kevin, Bertotti, G., & Nick, H. M. (2016b). The impact of different aperture distribution models and critical stress criteria on equivalent permeability in fractured rocks. *Journal of Geophysical Research: Solid Earth*, *121*(5), 4045–4063. https://doi.org/10.1002/2015JB012657

Bisdom, Kevin, Bertotti, G., Nick, H. M., Bertotti holds, G., Bouaziz, S., Hamammi, A., van

Eijk, M., van der Voet, E., & Vaughan Vrije, R. (2016). A geometrically based method for predicting stress-induced fracture aperture and flow in discrete fracture networks A U T H O R S. *AAPG Bulletin*, *V*, *100*(7), 1075–1097. https://doi.org/10.1306/02111615127

Boersma, Q., Prabhakaran, R., Bezerra, F. H., & Bertotti, G. (2019). Linking natural fractures to karst cave development: A case study combining drone imagery, a natural cave network and numerical modelling. *Petroleum Geoscience*, *25*(4), 454–469. https://doi.org/10.1144/petgeo2018-151

Bonnet, E., Bour, O., Odling, N. E., Davy, P., Main, I., Cowie, P., & Berkowitz, B. (2001). Scaling of fracture systems in geological media. *Reviews of Geophysics*, *39*(3), 347–383. https://doi.org/10.1029/1999RG000074

Boro, H, Bertotti, G., & Hardebol, N. J. (2013). Distributed fracturing affecting isolated carbonate platforms, the Latemar Platform Natural Laboratory (Dolomites, North Italy). *Marine and Petroleum Geology*, *40*, 69–84. https://doi.org/10.1016/j.marpetgeo.2012.09.012

Boro, Herman. (2012). *Fracturing , Physical Properties and Flow Patterns in Isolated Carbonate Platforms*.

BOSELLINI, A. (1984). Progradation geometries of carbonate platforms: examples from the Triassic of the Dolomites, northern Italy. *Sedimentology*, *31*(1), 1–24. https://doi.org/10.1111/j.1365-3091.1984.tb00720.x

Bosellini, A., Gianolla, P., & Stefani, M. (2003). Geology of the Dolomites, an introduction. *Episodes*, *26*(3), 43. file:///D:/Dottorato back-up 04-04-2013/Bibliografia/Areas/Tethyan Realm/Southern Alps/Dolomites

Bourbiaux, B., Basquet, R., Daniel, J. M., Hu, L. Y., Jenni, S., Lange, G., & Rasolofosaon, P. (2005). Fractured reservoirs modelling: a review of the challenges and some recent solutions. *First Break*, *23*(1087). https://doi.org/10.3997/1365-2397.2005018

Bourbiaux, Bernard, Basquet, R., Cacas, M. C., Daniel, J. M., & Sarda, S. (2002). An integrated workflow to account for multi-scale fractures in reservoir simulation models: Implementation and benefits. *Society of Petroleum Engineers - Abu Dhabi International Petroleum Exhibition and Conference 2002, ADIPEC 2002*. https://doi.org/10.2523/78489-ms

Bruhn, C. H. L., Pinto, A. C. C., Johann, P. R. S., Branco, C. C. M., Salomão, M. C., & Freire, E. B. (2017). Campos and Santos basins: 40 Years of reservoir characterization and management of shallow- to ultra-deep water, post- and pre-salt reservoirs - Historical overview and future challenges. *OTC Brasil 2017*, 327–350. https://doi.org/10.4043/28159-ms

Bruna, P. O., Lavenu, A. P. C., Matonti, C., & Bertotti, G. (2019). Are stylolites fluid-flow efficient features? *Journal of Structural Geology*. https://doi.org/10.1016/j.jsg.2018.05.018

Christ, N., Immenhauser, A., Amour, F., Mutti, M., Preston, R., Whitaker, F. F., Peterhänsel, A., Egenhoff, S. O., Dunn, P. A., & Agar, S. M. (2012). Triassic Latemar cycle tops - Subaerial exposure of platform carbonates under tropical arid climate. *Sedimentary Geology*, *265–266*, 1–29. https://doi.org/10.1016/j.sedgeo.2012.02.008

Cottereau, N., Garcia, M. H., Gosselin, O. R., & Vigier, L. (2010). *Effective Fracture Network*

*Permeability: Comparative Study of Calculation Methods*. 1–31. https://doi.org/10.2118/131126-ms

de Dreuzy, J.-R., Davy, P., & Bour, O. (2002). Hydraulic properties of two-dimensional random fracture networks following power law distributions of length and aperture. *Water Resources Research*, *38*(12), 121–129. https://doi.org/10.1029/2001WR001009

Doglioni, C. (1988). Examples of strike-slip tectonics on platform-basin margins. *Tectonophysics*, *156*(3–4), 293–302. https://doi.org/10.1016/0040-1951(88)90066-2

Egenhoff, S. O., Peterhänsel, A., Bechstädt, T., Zühlke, R., & Grötsch, J. (1999). Facies architecture of an isolated carbonate platform: Tracing the cycles of the Latemar (Middle Triassic, northern Italy). *Sedimentology*, *46*(5), 893–912. https://doi.org/10.1046/j.1365-3091.1999.00258.x

Emmerich, A., Zamparelli, V., Bechstädt, T., & Zühlke, R. (2005). The reefal margin and slope of a Middle Triassic carbonate platform: The Latemar (Dolomites, Italy). *Facies*, *50*(3–4), 573–614. https://doi.org/10.1007/s10347-004-0033-6

Furtado, C. P. Q., Medeiros, W. E., Borges, S. V., Lopes, J. A. G., Bezerra, F. H. R., Lima-Filho, F. P., Maia, R. P., Bertotti, G., Auler, A. S., & Teixeira, W. L. E. (2022). The influence of subseismic-scale fracture interconnectivity on fluid flow in fracture corridors of the Brejões carbonate karst system, Brazil. *Marine and Petroleum Geology*, *141*(January), 105689. https://doi.org/10.1016/j.marpetgeo.2022.105689

Gaetani, M., Fois, E., Jadoul, F., & Nicora, A. L. D. A. (1981). Nature and evolution of middle triassic carbonate buildups in the dolomites (Italy). *Marine Geology*, *44*, 25–57.

Gale, J. F. W., Lander, R. H., Reed, R. M., & Laubach, S. E. (2010). Modeling fracture porosity evolution in dolostone. *Journal of Structural Geology*, *32*(9), 1201–1211. https://doi.org/10.1016/j.jsg.2009.04.018

Garland, J., Neilson, J., Laubach, S. E., & Whidden, & K. J. (2012). Advances in carbonate exploration and reservoir analysis. *Geological Society of London, Special Publication*, *370*, 1–15. https://doi.org/10.1144/SP370.15

Geiger, S., & MatthäI, S. (2014). What can we learn from high-resolution numerical simulations of single- and multi-phase fluid flow in fractured outcrop analogues? *Geological Society Special Publication*, *374*(1), 125–144. https://doi.org/10.1144/SP374.8

Goldhammer, R., & Harris, M. (1989). *Eustatic controls on the stratigraphy and geometry of the Latemar buildup (Middle Triassic), the Dolomites of northern Italy*. http://archives.datapages.com/data/sepm_sp/SP44/Eustatic_Controls_on_the_Stratigraphy_.pdf

Goldhammer, R. K., Dunn, P. A., & Hardie, L. A. (1990). Depositional cycles, composite sea-level changes, cycle stacking patterns, and the hierarchy of stratigraphic forcing: Examples from Alpine Triassic platform carbonates. *Bulletin of the Geological Society of America*, *102*(5), 535–562. https://doi.org/10.1130/0016-7606(1990)102<0535:DCCSLC>2.3.CO;2

Hardebol, N. J., Maier, C., Nick, H., Geiger, S., Bertotti, G., & Boro, H. (2015). Multiscale fracture network characterization and impact on flow: A case study on the Latemar carbonate platform. *Journal of Geophysical Research: Solid Earth*, *120*(12), 8197–8222.

https://doi.org/10.1002/2015JB012608.Received

Harris, M. T. (1994). The Foreslope and Toe-of-Slope Facies of the Middle Triassic Latemar Buildup (Dolomites, Northern Italy). *Sedimentary Research*, 132–145.

Heffer, K. J., & Koutsabeloulis, N. C. (1995). Stress effects on reservoir flow: Numerical modelling used to reproduce field data. *Geological Society Special Publication*, *84*, 81–88. https://doi.org/10.1144/GSL.SP.1995.084.01.09

Heidbach, O., Rajabi, M., Cui, X., Fuchs, K., Müller, B., Reinecker, J., Reiter, K., Tingay, M., Wenzel, F., Xie, F., Ziegler, M. O., Zoback, M. Lou, & Zoback, M. (2018). The World Stress Map database release 2016: Crustal stress pattern across scales. *Tectonophysics*, *744*(April), 484–498. https://doi.org/10.1016/j.tecto.2018.07.007

Hooker, J. N., Laubach, S. E., & Marrett, R. (2013). Fracture-aperture sizedfrequency, spatial distribution, and growth processes in strata-bounded and non-strata-bounded fractures, cambrian mesón group, NW argentina. *Journal of Structural Geology*. https://doi.org/10.1016/j.jsg.2013.06.011

Hooker, J. N., Laubach, S. E., & Marrett, R. (2014). A universal power-law scaling exponent for fracture apertures in sandstones. *GSA Bulletin*, *126*(9–10), 1340–1362. https://doi.org/10.1130/B30945.1

Igbokwe, O. A., Mueller, M., Abah, O., Bertotti, G., & Immenhauser, A. (2018). Morphological changes of carbonate deformed clasts in a neogene fault zone. *3rd EAGE Workshop on Naturally Fractured Reservoirs*, *2018-Febru*. https://doi.org/10.3997/2214-4609.201800040

Igbokwe, Onyedika Anthony, Bertotti, G., Mueller, M., Chima, K. I., & Immenhauser, A. (2022). *Geometries, Driving Factors, And Connectivity Of Background Fractures At The Latemar Carbonate Platform (N. Italy): Relevance For Subsurface Reservoir Modelling*. https://doi.org/10.1002/ESSOAR.10511547.1

Igbokwe, Onyedika Anthony, Mueller, M., Bertotti, G., Timothy, J. J., Abah, O., & Immenhauser, A. (2020). Morphology and topology of dolostone lithons in the regional Carboneras Fault Zone, Southern Spain. *Journal of Structural Geology*, *137*. https://doi.org/10.1016/j.jsg.2020.104073

Jacquemyn, C., El Desouky, H., Hunt, D., Casini, G., & Swennen, R. (2014). Dolomitization of the Latemar platform: Fluid flow and dolomite evolution. *Marine and Petroleum Geology*, *55*, 43–67. https://doi.org/10.1016/j.marpetgeo.2014.01.017

Jacquemyn, C., Huysmans, M., Hunt, D., Casini, G., & Swennen, R. (2015). Multi-scale three-dimensional distribution of fracture-and igneous intrusion-controlled hydrothermal dolomite from digital outcrop model, Latemar platform, Dolomites, northern Italy. *AAPG Bulletin*, *V*, *99*(5), 957–984. https://doi.org/10.1306/10231414089

Jonoud, S., & Jackson, M. D. (2008). New criteria for the validity of steady-state upscaling. *Transport in Porous Media*, *71*(1), 53–73. https://doi.org/10.1007/s11242-007-9111-x

Khodaei, M., Biniaz Delijani, E., Dehghan, A. N., Hajipour, M., & Karroubi, K. (2021). Stress/strain variability in fractured media: a fracture geometric study. *Geotechnical and Geological Engineering*, 1–20. https://doi.org/10.1007/s10706-021-01838-4

Laubach, S. E. (2003). Practical approaches to identifying sealed and open fractures. *American Association of Petroleum Geologists Bulletin*, *87*(4), 561–579.

https://doi.org/10.1306/11060201106

Lei, Q., Latham, J. P., & Tsang, C. F. (2017). The use of discrete fracture networks for modelling coupled geomechanical and hydrological behaviour of fractured rocks. In *Computers and Geotechnics* (Vol. 85, pp. 151–176). Elsevier Ltd. https://doi.org/10.1016/j.compgeo.2016.12.024

Lei, Q., Latham, J. P., Xiang, J., & Tsang, C. F. (2015). Polyaxial stress-induced variable aperture model for persistent 3D fracture networks. *Geomechanics for Energy and the Environment*, *1*, 34–47. https://doi.org/10.1016/j.gete.2015.03.003

Lei, Q., Latham, J. P., Xiang, J., Tsang, C. F., Lang, P., & Guo, L. (2014). Effects of geomechanical changes on the validity of a discrete fracture network representation of a realistic two-dimensional fractured rock. *International Journal of Rock Mechanics and Mining Sciences*, *70,* 507–523. https://doi.org/10.1016/j.ijrmms.2014.06.001

Leonhart, D., Timothy, J. J., & Meschke, G. (2017). Cascade Continuum Micromechanics model for the effective permeability of solids with distributed microcracks: Comparison with numerical homogenization. *Mechanics of Materials*, *115*, 64–75. https://doi.org/10.1016/j.mechmat.2017.09.001

Makedonska, N., Hyman, J. D., Karra, S., Painter, S. L., Gable, C. W., & Viswanathan, H. S. (2016). Evaluating the effect of internal aperture variability on transport in kilometer scale discrete fracture networks. *Advances in Water Resources*, *94*, 486–497. https://doi.org/10.1016/j.advwatres.2016.06.010

Marangon, A., Gattolin, G., Della Porta, G., & Preto, N. (2011). The Latemar: A flat-topped, steep fronted platform dominated by microbialites and synsedimentary cements. *Sedimentary Geology*, *240*(3–4), 97–114. https://doi.org/10.1016/j.sedgeo.2011.09.001

Matthäi, S. K. (2003). Fluid flow and (reactive) transport in fractured and faulted rock. *Journal of Geochemical Exploration*, *78–79*, 179–182. https://doi.org/10.1016/S0375-6742(03)00094-3

Matthäi, S. K., & Belayneh, M. (2004). Fluid flow partitioning between fractures and a permeable rock matrix. *Geophysical Research Letters*, *31*(7). https://doi.org/10.1029/2003GL019027

Matthai, S. K., & Nick, H. M. (2009). Upscaling two-phase flow in naturally fractured reservoirs. *AAPG Bulletin*, *93*(11), 1621–1632. https://doi.org/10.1306/08030909085

McNamara, D. D., Massiot, C., Lewis, B., & Wallis, I. C. (2015). Heterogeneity of structure and stress in the RotokawaGeothermal F ield, New Zealand. *Journal of Geophysical Research: Solid Earth*, 3782–3803. https://doi.org/10.1002/2015JB012608.Received

Min, K.-B., Rutqvist, J., Tsang, C. F., & Jing, L. (2004). Stress-dependent permeability of fractured rock masses: A numerical study. *International Journal of Rock Mechanics and Mining Sciences*, *41*(7), 1191–1210. https://doi.org/10.1016/j.ijrmms.2004.05.005

Narr, W., Schechter, D. S., & Thompson, L. B. (2006). *Naturally Fractured Reservoir Characterization*.

Olson, Jolson E. (2007). Fracture aperture, length and pattern geometry development under biaxial: A numerical study with applications to natural, cross-jointed systems. *Geological Society Special Publication, 289*(2001), 123–142. https://doi.org/10.1144/SP289.8

Olson, Jon E. (2003). Sublinear scaling of fracture aperture versus length: An exception or the rule? *Journal of Geophysical Research: Solid Earth*, *108*(B9), 2413. https://doi.org/10.1029/2001jb000419

Pascal, C., & Cloetingh, S. A. P. L. (2009). Gravitational potential stresses and stress field of passive continental margins: Insights from the south-Norway shelf. *Earth and Planetary Science Letters*, *277*(3–4), 464–473. https://doi.org/10.1016/j.epsl.2008.11.014

Peacock, D. C. P. (2009). A review of Alpine deformation and stresses in southern England. *Bollettino Della Societa Geologica Italiana*, *128*(2), 307–316. https://doi.org/10.3301/IJG.2009.128.2.307

Preto, N., Franceschi, M., Gattolin, G., Massironi, M., Riva, A., Gramigna, P., Bertoldi, L., & Nardon, S. (2011). The Latemar: A Middle Triassic polygonal fault-block platform controlled by synsedimentary tectonics. *Sedimentary Geology*, *234*(1–4), 1–18. https://doi.org/10.1016/j.sedgeo.2010.10.010

Rotevatn, A., Buckley, S. J., Howell, J. A., & Fossen, H. (2009). Overlapping faults and their effect on fluid flow in different reservoir types: A LIDAR-based outcrop modeling and flow simulation study. *AAPG Bulletin*, *93*(3), 407–427. https://doi.org/10.1306/09300807092

Sanderson, D. J., & Nixon, C. W. (2015). The use of topology in fracture network characterization. *Journal of Structural Geology*, *72*, 55–66. https://doi.org/10.1016/j.jsg.2015.01.005

Scholz, C. H. (2010). A note on the scaling relations for opening mode fractures in rock. *Journal of Structural Geology*, *32*(10), 1485–1487. https://doi.org/10.1016/j.jsg.2010.09.007

Stephansson, O., Ljunggren, C., & Jing, L. (1991). Stress measurements and tectonic implications for Fennoscandia. *Tectonophysics*, *189*(1–4), 317–322. https://doi.org/10.1016/0040-1951(91)90504-L

Timothy, J. J., & Meschke, G. (2016). Cascade Lattice Micromechanics Model for the Effective Permeability of Materials with Microcracks. *Journal of Nanomechanics and Micromechanics*. https://doi.org/10.1061/(asce)nm.2153-5477.0000113

Whitaker, F. F., Felce, G. P., Benson, G. S., Amour, F., Mutti, M., & Smart, P. L. (2014). Simulating flow through forward sediment model stratigraphies: Insights into climatic control of reservoir quality in isolated carbonate platforms. *Petroleum Geoscience*, *20*(1), 27–40. https://doi.org/10.1144/petgeo2013-026

Wilson, C. E., Aydin, A., Durlofsky, L. J., Sagy, A., Emily, E., Kreylos, O., & Kellogg, L. H. (2011). *From outcrop to flow simulation : Constructing discrete fracture models from a LIDAR survey*. *11*(11), 1883–1905. https://doi.org/10.1306/03241108148

Yale, D. P. (2003). Fault and stress magnitude controls on variations in the orientation of in situ stress. *Geological Society Special Publication*, *209*, 55–64. https://doi.org/10.1144/GSL.SP.2003.209.01.06

Zhang, X., & Sanderson, D. J. (1996). Effects of stress on the two-dimensional permeability tensor of natural fracture networks. *Geophysical Journal International*, *125*(3), 912–924. https://doi.org/10.1111/j.1365-246X.1996.tb06034.x

Zoback, M. D. (2007). *Reservoir Geomechanics*. Cambridge University Press The Edinburgh

Building, Cambridge CB2 8RU, UK. https://doi.org/10.18814/epiiugs/2009/v32i3/009

## Declaration of interests

☒ The authors declare that they have no known competing financial interests or personal relationships that could have appeared to influence the work reported in this paper.

## Author Contribution Statement

The first author named is the lead and corresponding author. All other authors are listed according to their contributions. We describe contributions to the paper using Contribution Roles Taxonomy (CRediT)[2] as follows:

**Onyedika Anthony Igbokwe:** Conceptualization, Methodology, Software, Formal analysis, Investigation, Data curation, Writing- Original draft preparation, Visualization, Project administration. **Jithender J. Timothy**: Data curation, Writing- Reviewing and Editing, Validation. **Ashwani Kumar**: Investigation, Software, Resources, Data curation. ***Xiao Yan:*** Software, Validation, Data curation, Formal analysis. **Mathias Mueller:** Resources, Data curation. **Alessandro Verdecchia**: Resources, Data curation. **Günther Meschke:** Supervision, Project administration. **Adrian Immenhauser:** Supervision, Writing- Reviewing and Editing, Validation, Project administration.

[2] Accessed from https://www.elsevier.com/authors/policies-and-guidelines/credit-author-statement (Sept. 20, 2022)

## Figures

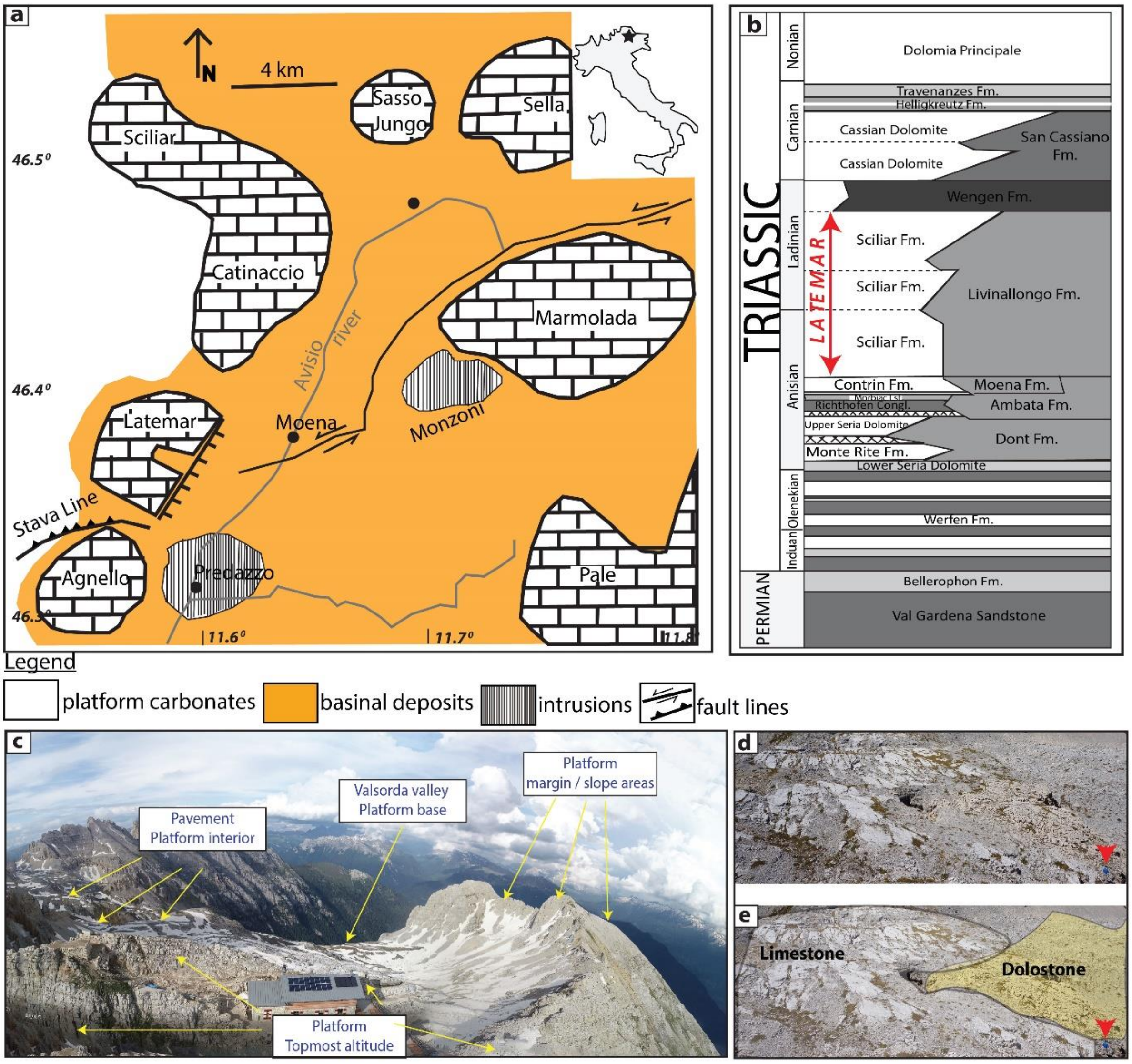


**Figure 1. (A)** Overview of the Latemar and the neighbouring Ladinian carbonate buildups (or platforms) and Upper Ladinian intrusions of the Dolomites (modified after Jacquemyn et al., 2014, 2015). **(B)** Simplified stratigraphic chart of the Dolomite Mountains, modified after Jacquemyn et al., 2014. **(D)** Drone image showing the general overview of the horse-shoe shape of the Latemar buildups. The geometry and topology of the outcrops pointed with arrows have been presented in Igbokwe et al. (2022). **(E)** Drone images acquired from the outcrop pavement at platform interior.

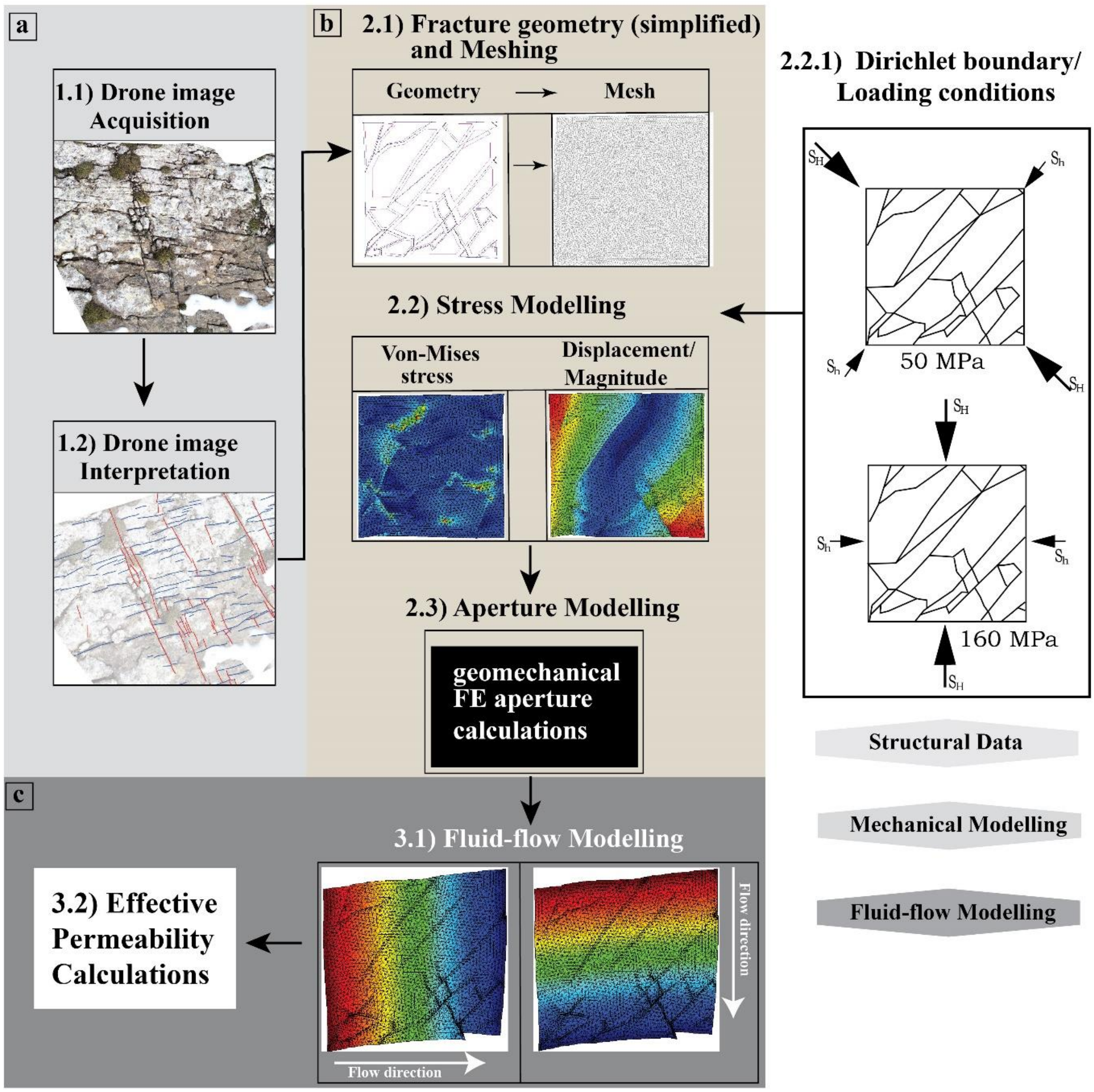


**Figure 2.** Workflow for obtaining flow-base effective permeability using acquired drone images from outcropping fracture networks. A) (Phase 1.1) Drone imagery, photogrammetry and (Phase 1.2) fracture interpretation and digitization (the illustration shown is a Fracture Sub-Sample (FSS) with ~ 2 x 2 m dimension). B) (Phase 2.1) Simplifying and converting the interpreted fracture network geometry to element geometry and, then, meshing, (Phase 2.2) local stress modelling, (Phase 2.3) geomechanical finite-element fracture-aperture modelling and calculations. C) (Phase 3.1) Fluid-flow modelling, considering "uncoupled" conditions and (Phase 3.2) effective permeability calculations.

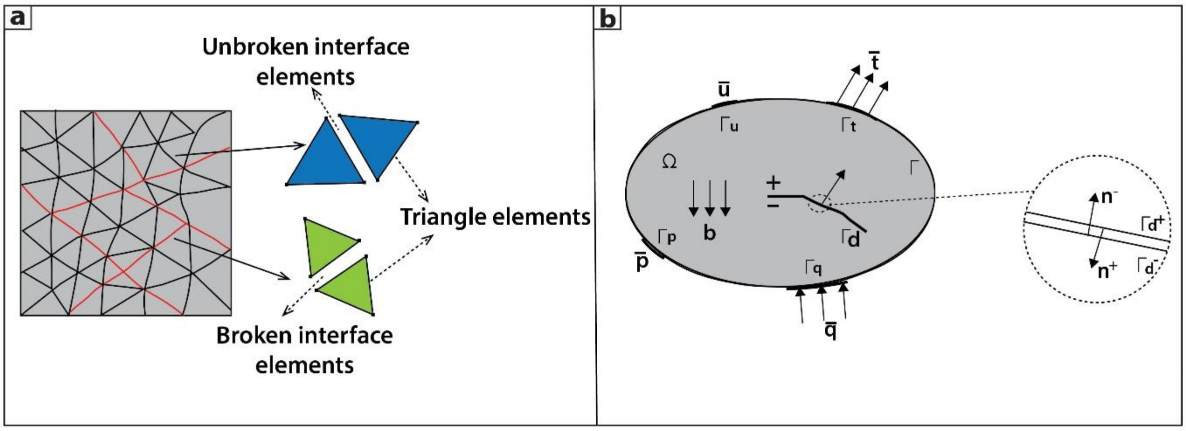


**Figure 3.** (A) Representation of a fractured rock using triangle elements and embedded zero-thickness interface elements in the solid model. (B) Boundary conditions of the porous medium **Ω**, including the geomechanical discontinuity $\Gamma_d$

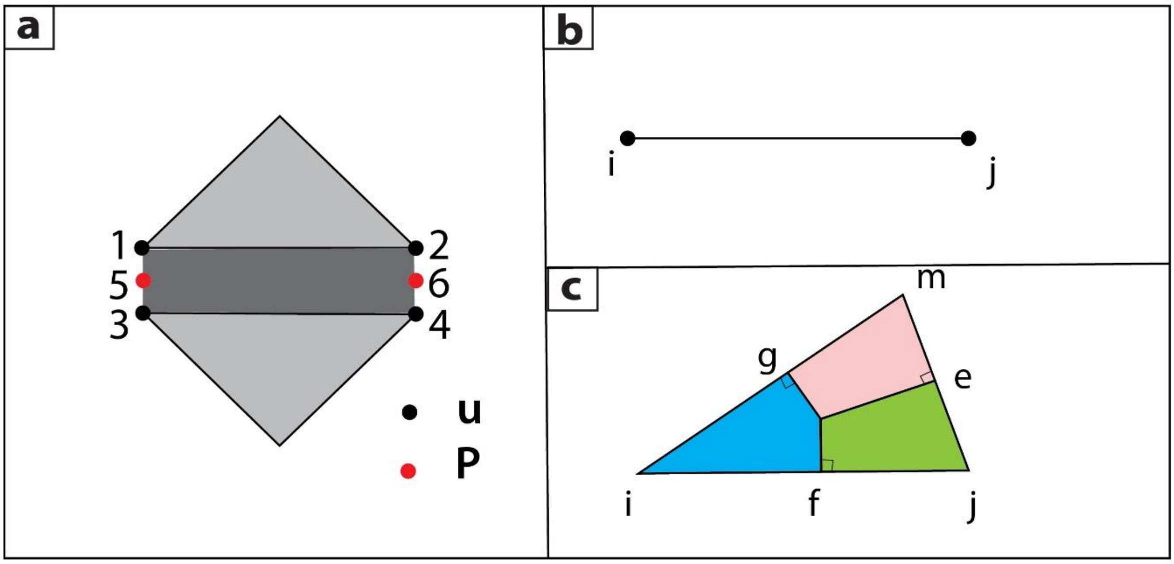


**Figure 4.** The computational discretization model. (A) the thickness of the interface element with hydromechanical coupling. (B) Fracture (Pipe) equivalence of idealized 1-D fracture. (c) Fracture (Pipe) equivalence of 2-D porous medium

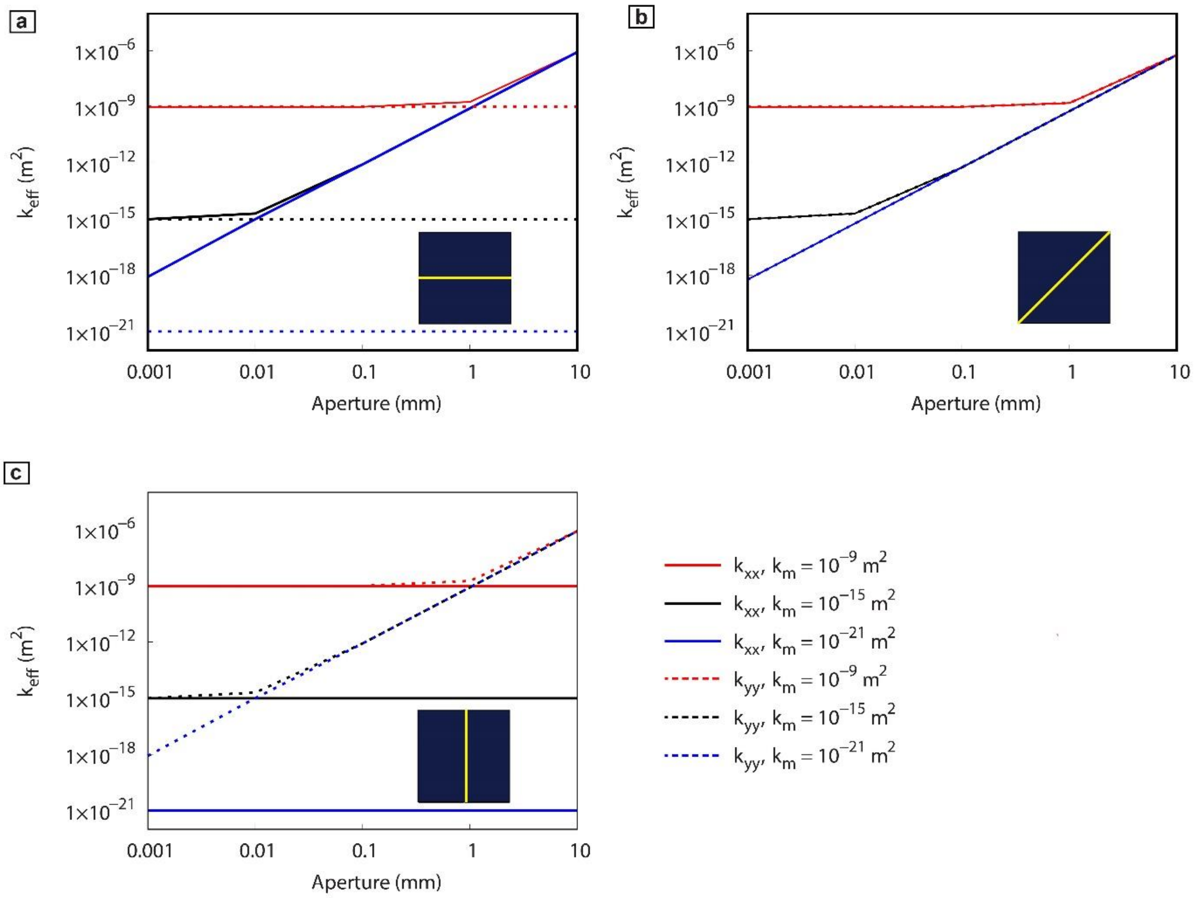


**Figure 5.** The effective permeability with different fracture aperture and rock matrix intrinsic permeability for single fracture (see embedded block) with different inclination degrees (a) 0°, (b) 45° and (c) 90°.

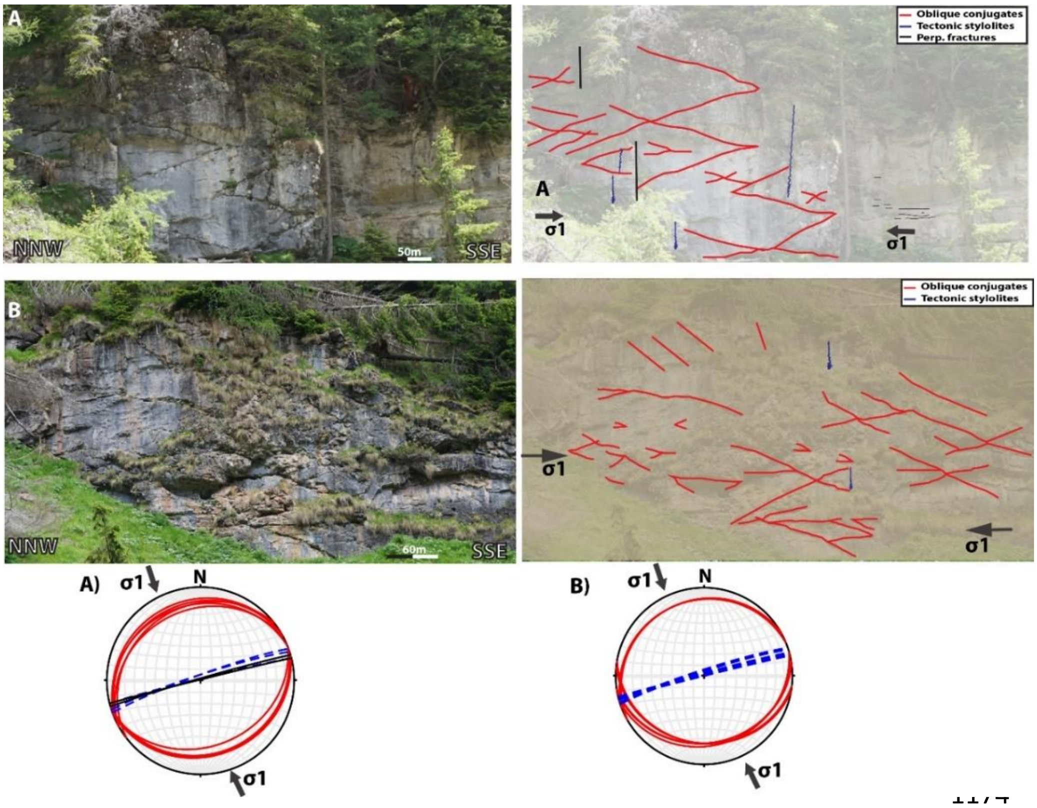


**Figure 6.** Sub-vertical outcrops exposed at the base of the Latemar. A and B) show reverse conjugate fault with low-angle SSE - and ENE dipping fractures and a horizontal intersection. The stereoplots show bedding-perpendicular stylolites and σ1 striking approximately WSW-ENE and NW-SE to NNW-SSE direction, respectively.

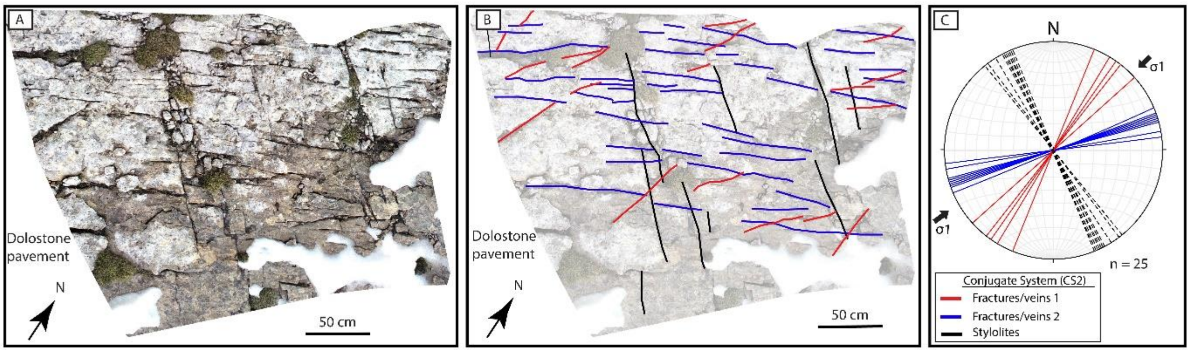


**Figure 7.** Sub-horizontal (pavement) outcrop exposed at the flat-topped Latemar. A and B) show high-resolution 2D outcrop orthorectified photograph and digitized fracture map. C) The stereoplots show σ1 striking approximately NW-SE to NNW-SSE direction.

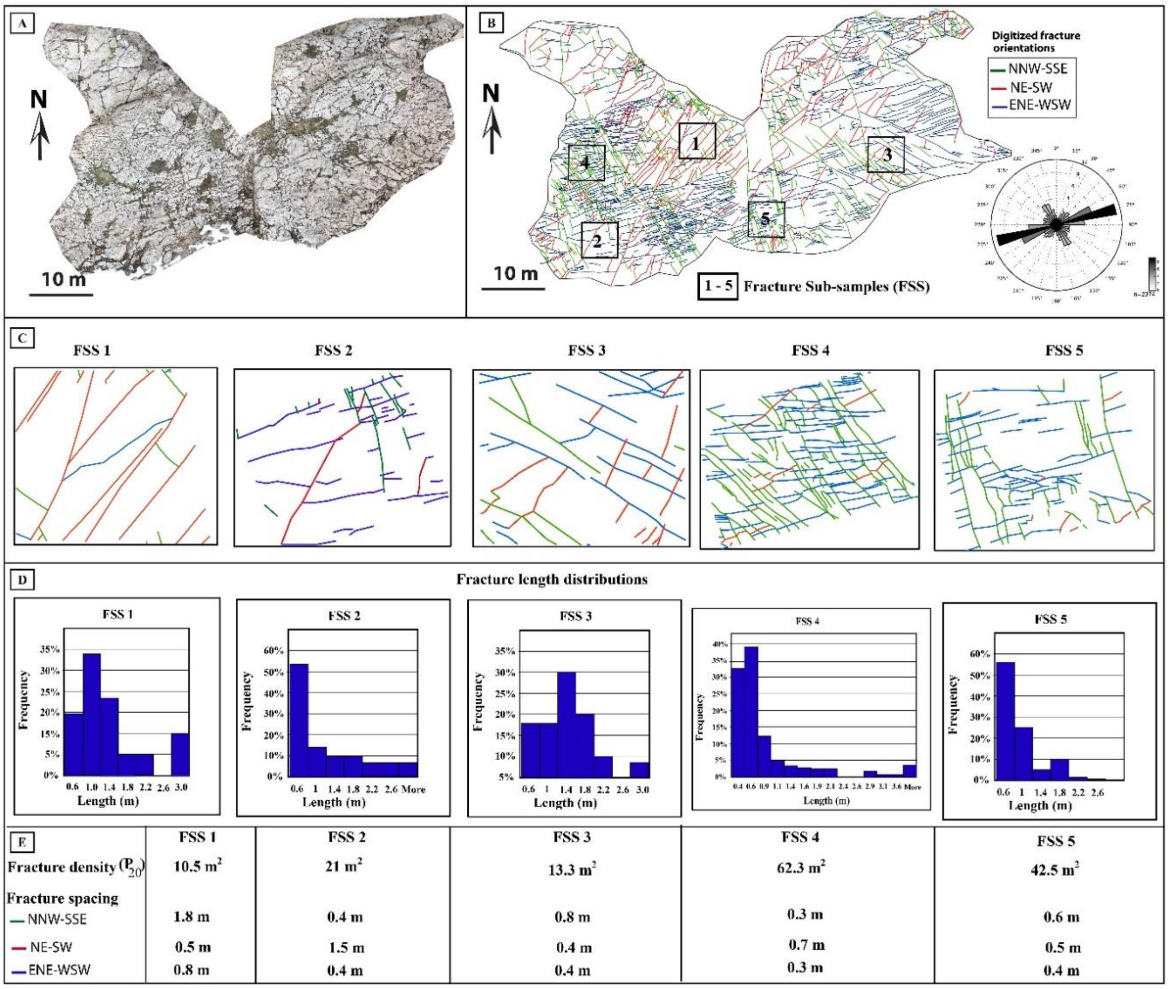


**Figure 8.** Original outcrop model with interpreted fractures, from where the five FSS were extracted. A) High-resolution 2D outcrop orthorectified photograph. B) Digitized sub-horizontal (pavement) in the Latmar with the position of the five outcrop windows, including the stereoplot of more than 2000 fracture orientations. C) The five fracture models. D) Length distribution of the five fracture models. E) Fracture geometry, including density and spacing values of the five outcrop models.

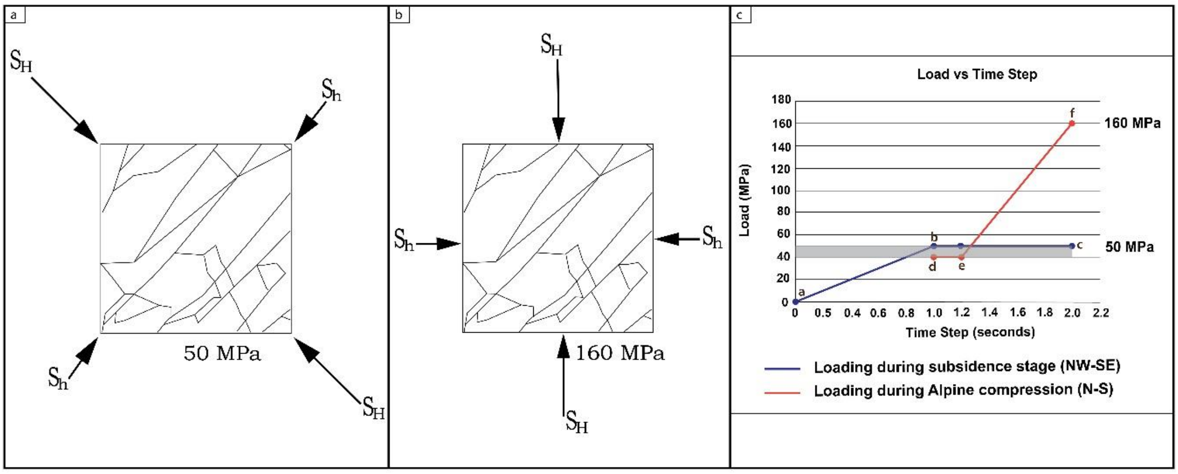


**Figure 9.** Quasi-static loading scenarios of the two tectonic stresses. A) The first stage loading reflects the subsidence deformation stress from the NW-SE direction and has a maximum load of 50 MPa. B) The second stage loading, representing the Alpine deformation stress from the N-S direction, is applied (added), while the loading of 50 MPa is maintained until a maximum of 160 MPa is reached. C) The plot of load against Time Steps. The first stage loading of 50 MPa corresponds to the line a-b-c (blue curve), whereas the second stage loading of 160 MPa corresponds to the line d-e-f (orange curve). The grey bar indicates that some stresses during the first loading were still active and became more significant during the second loading scenario.

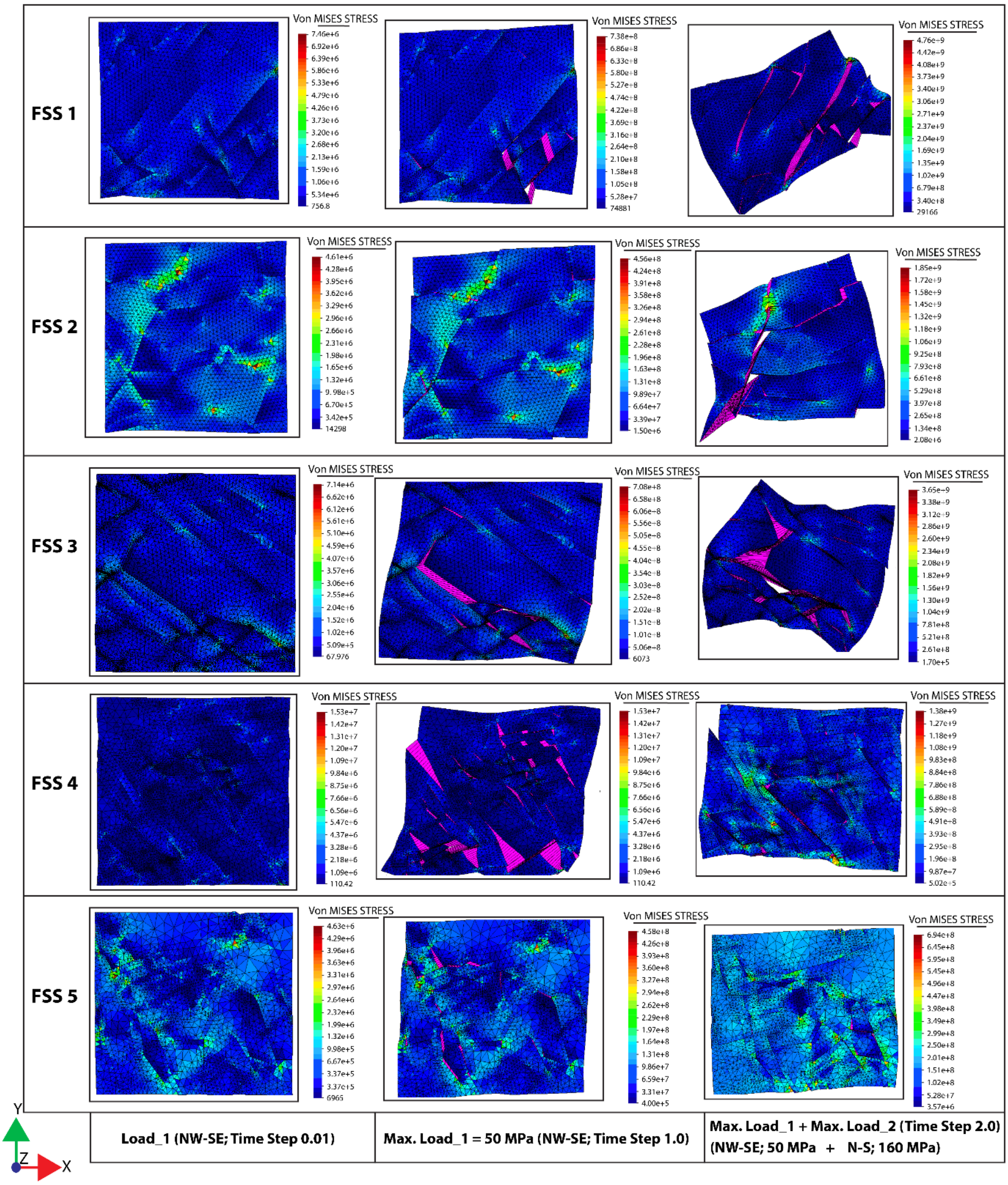


**Figure 10.** Von-Mises stress distribution (Pa) in the fractured rock domain (FSS 1 through FSS 5) under different loading conditions and orientations at Time Steps (0.01, 1.0, and 2.0). Note that the deformation scale is x10. The stress colour spectra are the same for all figures.

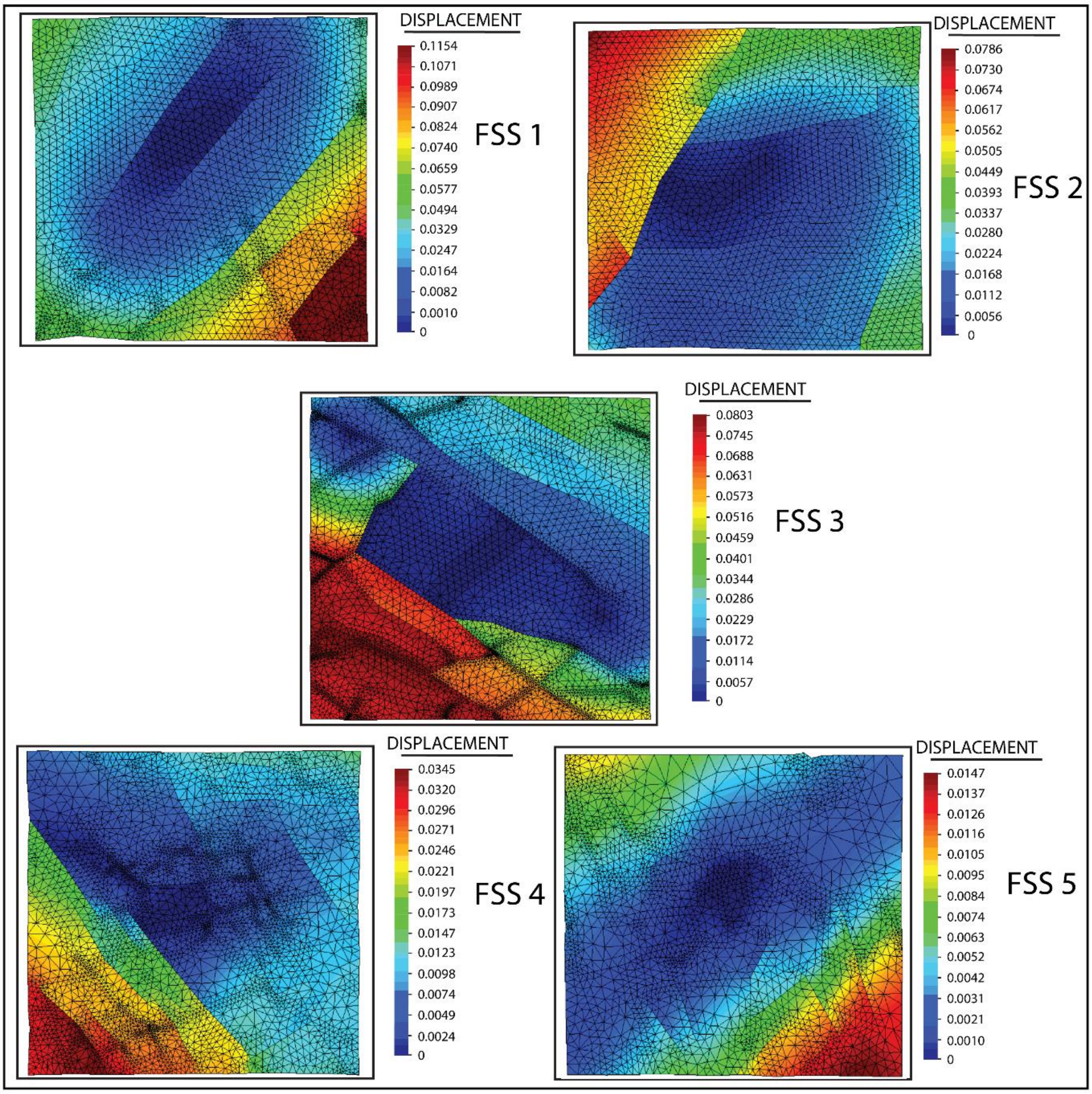


**Figure 11**. Distribution of actual displacement magnitude under the two tectonic stress conditions for FSS1 through FSS5, when the Time Step is 2. Units are in meters, and deformations are slightly magnified. Notice the varied displacements across the FSSs.

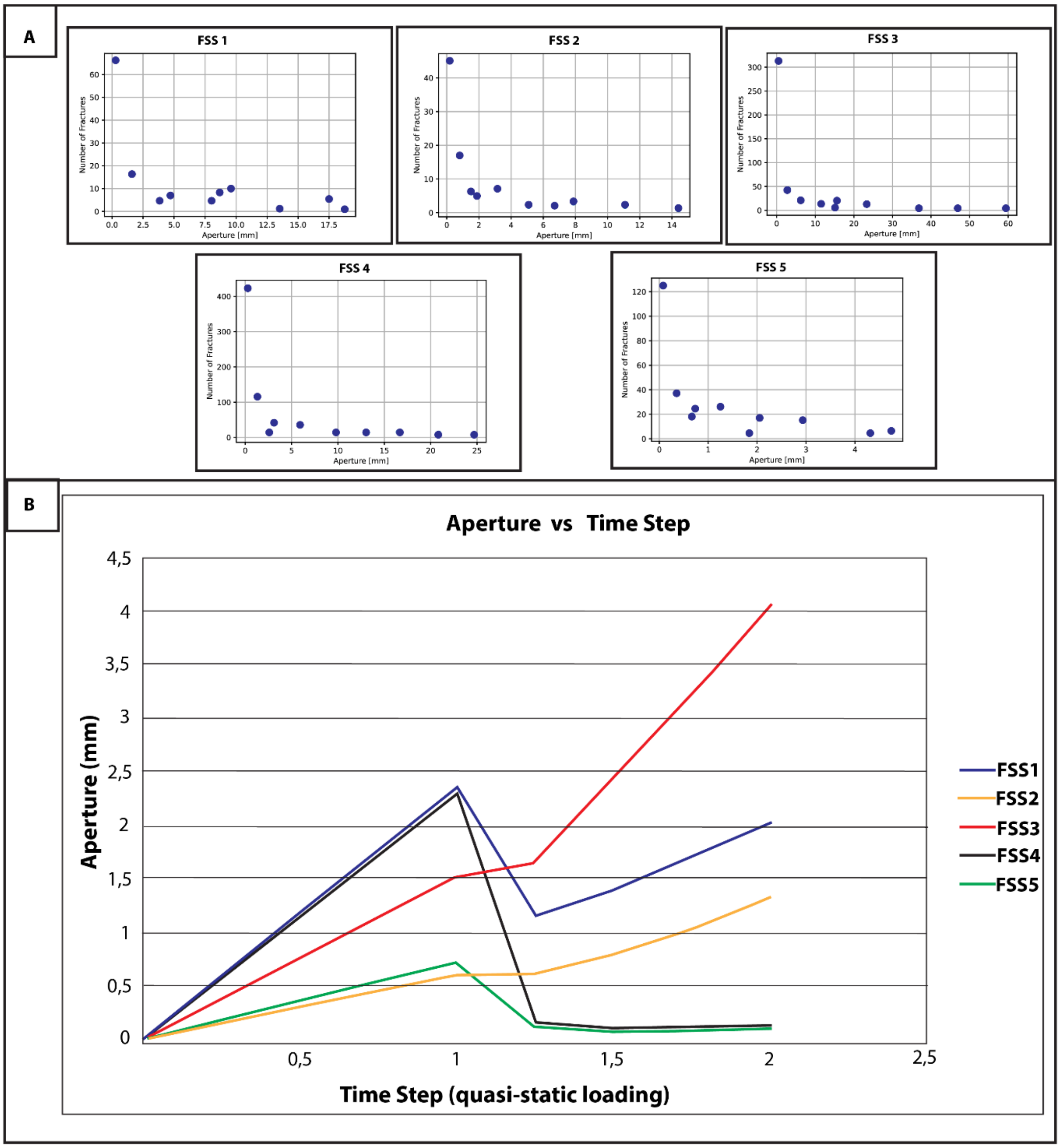


**Figure 12**. A) Distribution of fracture aperture under the two horizontal stress orientations. B) The relationship between aperture and mechanical loading conditions. Note that the Time is analogous to quasi-static loading conditions.

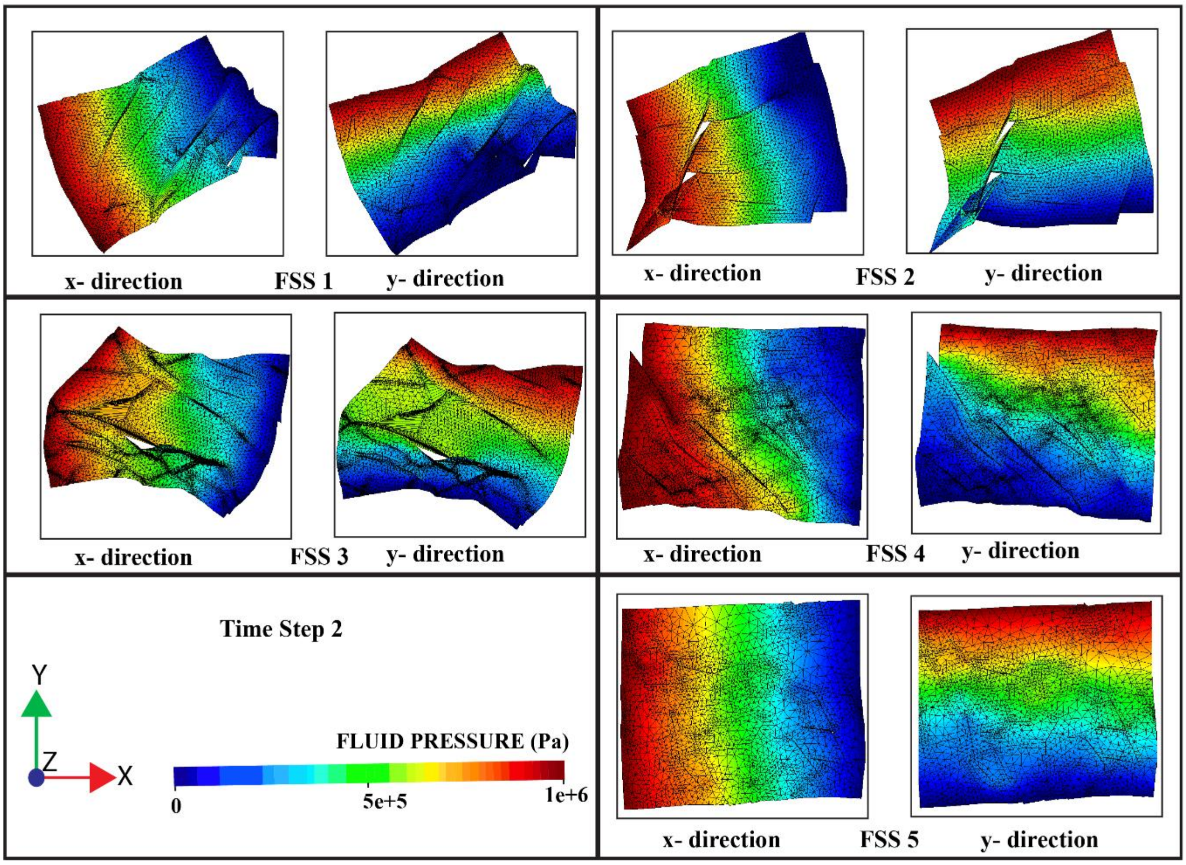


**Figure 13**. Contours of the fluid pressure gradient (Pa), obtained for a fluid pore pressure *p* at Time Step 2 (see Fig. 9 for the loading conditions), in the x- and y- directions. The matrix permeability is given as 2 x 10$^{-}$15 m$^{2}$

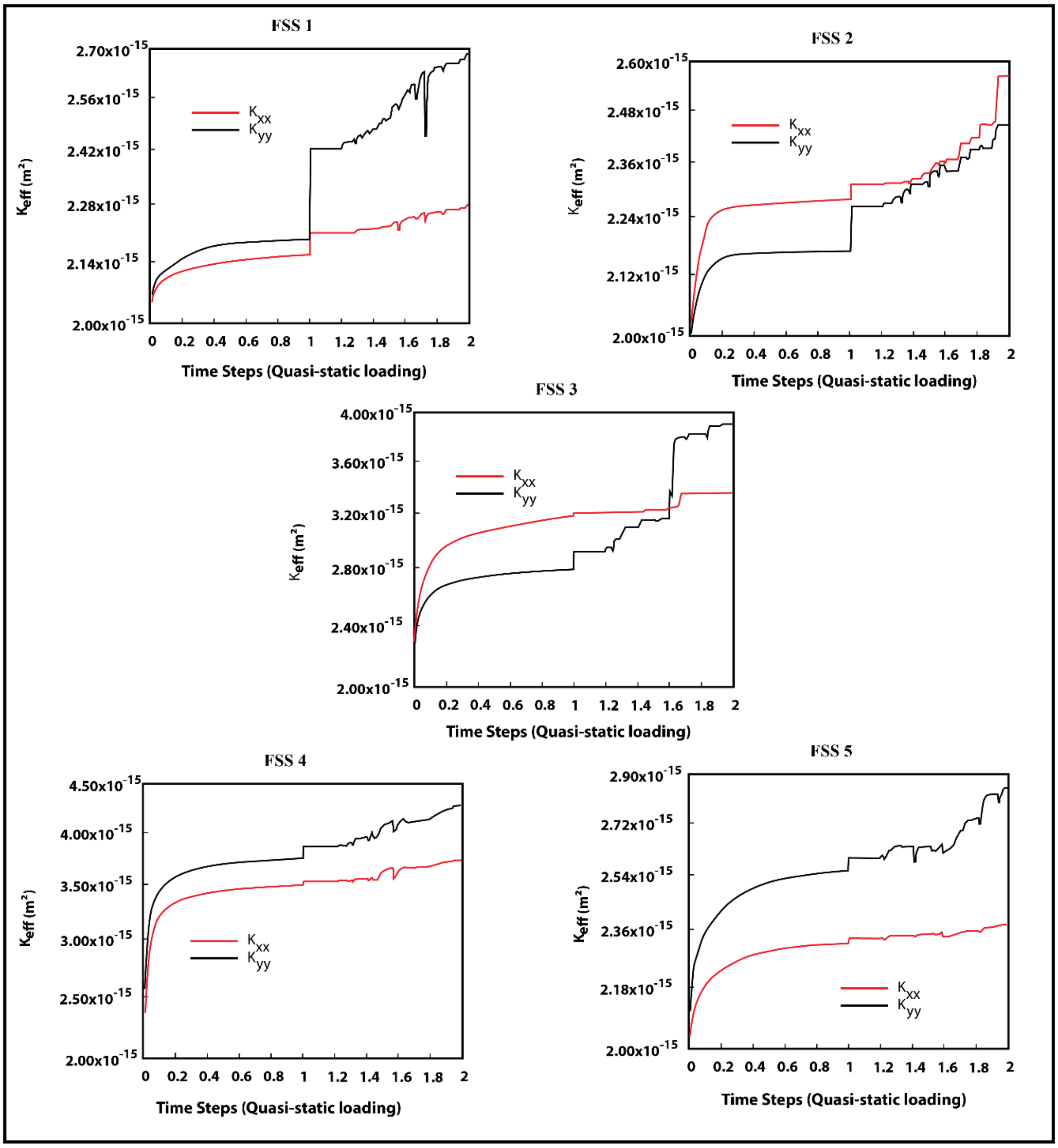


**Figure 14**. The Effective permeability values are plotted against the loading conditions for FSS1 through FSS5. The FSS 1 through 3 show significant “jump in permeabilitiy values” at Time Step 1 when the second quasi-static loading commences.

## Tables

**Table 1.** Essential model parameters applied for stress calculations. Adapted from Bertotti et al. (2017)

| | | Average data | Data range |
|---|---|---|---|
| Surface Tension ($Jm^{-2}$) | $Y$ | 0.27 | 0.27 |
| Young's Modulus (GPa) | $E$ | 25 | 15 – 45 |
| Poisson's ratio | $v$ | 0.3 | 0.25 – 0.3 |
| Rock density ($Kgm^{-3}$) | $\rho$ | 2200 | 2000 – 2700 |
| Tectonic Stress (MPa) | | 10 | 0 – 35 |

**Table 2**. Effective permeabilities, including permeability Tensor obtained at different loading scenarios

| | | Effective Permeability ($K_{eff}$) $K\ X10^{-15}\ (m^2)$ | | |
|---|---|---|---|---|
| | | Matrix permeability = 2.00 | | |
| | Time Steps | $K_{xx}$ | $K_{yy}$ | $K_{xx}/K_{yy}$ |
| **FSS 1** | 1 | 2.14 | 2.20 | 0.98 |
| **FSS 2** | 1 | 2.30 | 2.18 | 1.05 |
| **FSS 3** | 1 | 3.10 | 2.60 | 1.19 |
| **FSS 4** | 1 | 3.40 | 3.70 | 0.92 |
| **FSS 5** | 1 | 2.80 | 2.54 | 1.10 |
| **Average** | **1** | **2.75** | **2.64** | **1.04** |
| **FSS 1** | 2 | 2.28 | 2.70 | 0.84 |
| **FSS 2** | 2 | 2.42 | 2.56 | 0.95 |
| **FSS 3** | 2 | 3.28 | 3.90 | 0.84 |
| **FSS 4** | 2 | 3.50 | 4.20 | 0.83 |
| **FSS 5** | 2 | 2.36 | 2.84 | 0.83 |
| **Average** | **2** | **2.77** | **3.24** | **0.85** |